

On the probability distribution function of the mass surface density of molecular clouds. II

Jörg Fischera

Canadian Institute for Theoretical Astrophysics, University of Toronto, 60 St. George Street, Toronto, ON M5S3H8, Canada

Preprint online version: October 23, 2018

ABSTRACT

The probability distribution function (PDF) of the mass surface density of molecular clouds provides essential information about the structure of molecular cloud gas and condensed structures out of which stars may form. In general, the PDF shows two basic components: a broad distribution around the maximum with resemblance to a log-normal function, and a tail at high mass surface densities attributed to turbulence and self-gravity. In a previous paper, the PDF of condensed structures has been analyzed and an analytical formula presented based on a truncated radial density profile, $\rho(r) = \rho_c / (1 + (r/r_0)^2)^{n/2}$ with central density ρ_c and inner radius r_0 , widely used in astrophysics as a generalization of physical density profiles. In this paper, the results are applied to analyze the PDF of self-gravitating, isothermal, pressurized, spherical (Bonnor-Ebert spheres) and cylindrical condensed structures with emphasis on the dependence of the PDF on the external pressure p_{ext} and on the overpressure $q^{-1} = p_c/p_{\text{ext}}$, where p_c is the central pressure. Apart from individual clouds, we also consider ensembles of spheres or cylinders, where effects caused by a variation of pressure ratio, a distribution of condensed cores within a turbulent gas, and (in case of cylinders) a distribution of inclination angles on the mean PDF are analyzed. The probability distribution of pressure ratios q^{-1} is assumed to be given by $P(q^{-1}) \propto q^{-k_1} / (1 + (q_0/q)^\gamma)^{(k_1+k_2)/\gamma}$, where k_1 , γ , k_2 , and q_0 are fixed parameters. The PDF of individual spheres with overpressures below ~ 100 is well represented by the PDF of a sphere with an analytical density profile with $n = 3$. At higher pressure ratios, the PDF at mass surface densities $\Sigma \ll \Sigma(0)$, where $\Sigma(0)$ is the central mass surface density, asymptotically approaches the PDF of a sphere with $n = 2$. Consequently, the power-law asymptote at mass surface densities above the peak steepens from $P_{\text{sph}}(\Sigma) \propto \Sigma^{-2}$ to $P_{\text{sph}}(\Sigma) \propto \Sigma^{-3}$. The corresponding asymptote of the PDF of cylinders for the large q^{-1} is approximately given by $P_{\text{cyl}}(\Sigma) \propto \Sigma^{-4/3} (1 - (\Sigma/\Sigma(0))^{2/3})^{-1/2}$. The distribution of overpressures q^{-1} produces a power-law asymptote at high mass surface densities given by $\langle P_{\text{sph}}(\Sigma) \rangle \propto \Sigma^{-2k_2-1}$ (spheres) or $\langle P_{\text{cyl}}(\Sigma) \rangle \propto \Sigma^{-2k_2}$ (cylinders).

Key words. ISM: molecular clouds numerical methods: statistics, analytical

1. Introduction

The observed probability distribution function (PDF) of the mass surface density of molecular clouds suggests a combination of two separate components that produce a broad distribution around the peak, which is generally modeled using a log-normal function and a tail at high mass surface densities that often has a power-law form (e.g., Kainulainen et al. (2009); Kainulainen & Tan (2013); Schneider et al. (2012, 2013)). The broad distribution around the maximum is typically attributed to turbulence of the molecular gas, the tail to self-gravitating structures. The relative amount of gas in gravitationally bound structures seems to be indicative of the star formation rate in the cloud. The PDF of star-forming molecular clouds like Taurus or Ophiuchus, for example, is characterized by a strong tail that seems to be very low or absent in clouds with no apparent star formation, such as the 'Coalsack' (Kainulainen et al. 2009).

Images of the column densities of molecular clouds (Schneider et al. 2012; Kainulainen & Tan 2013) show that the high column density values are not randomly distributed within the cloud, but are indeed related to small regions, as expected for cold condensed structures surrounded

by warmer or more turbulent gas. In a previous paper (Fischera 2014, Paper I) the PDFs of spherical and cylindrical condensed structures have been analyzed assuming a truncated smooth radial density profile used in astrophysics as a generalization of physical density profiles. It was found that the PDF of such a profile can be described by a simple implicit analytical function. In Paper I, we showed how the geometric shape, the radial density profile, and the ratio $\rho_c/\rho(r_{\text{cl}})$ of the central density and the density at the peripheral regions affect the functional form of the PDF. For example, we found that the PDF of a sphere is truncated, while the PDF of a cylinder has a pole at the highest mass surface density.

In this paper, the results of Paper I are applied to analyze the PDF of isothermal self-gravitating pressurized spheres and cylinders as an approximation of individual condensations in giant molecular clouds. In the case of the global statistical properties of molecular clouds, the condensed structures probably show a variety of different physical conditions. The consequences of a number of distributions on the mean PDF are therefore also addressed.

The paper is divided into two main sections. In the first part (Sect. 2), the properties of the PDFs of individual spheres and cylinders are discussed. We show how the high-

est position and the asymptotes at low and high mass surface densities are affected by the pressure ratio p_c/p_{ext} and the external pressure p_{ext} surrounding the structures. The second part (Sect. 3) is about the properties of a mean PDF for a variety of distributions as they may apply to molecular clouds. In Sect. 3.2, we analyze the mean PDF of an ensemble of spheres and cylinders for a distribution of gravitational states. In Sect. 3.3, the effect caused by a distribution of cylinders with a variety of inclination angles is addressed, and in Sect. 3.4, we consider a mean PDF of cores that are uniformly distributed within a turbulent medium. The results are discussed in Sect. 4 and compared with observed PDFs, as derived by Kainulainen et al. (2009). The paper is summarized in Sect. 5.

2. Probability distribution function of the mass surface density of condensed structures

2.1. Density profile of the isothermal condensed structures

In Paper I, we have analyzed the one-point statistic for condensed spheres and cylinders assuming an analytical density profile given by

$$\rho(r) = \frac{\rho_c}{(1 + (r/r_0)^2)^{n/2}}, \quad (1)$$

where ρ_c is the central density and r_0 the inner radius. In the following we show how the density profile is related to the density profile of self-gravitating isothermal spheres, known as Bonnor-Ebert spheres (Ebert 1955; Bonnor 1956), and cylinders.

In isothermal clouds, the gas pressure and density are proportional, $p = K\rho$, where the proportionality constant is given by $K = kT/(\mu m_H)$, where k , T , μ , and m_H are the Boltzmann constant, the effective temperature, the mean molecular weight, and the mass of a hydrogen atom. For an idealized gas we have $K = c_s^2$, where c_s is the sound speed.

To analyze isothermal self-gravitating clouds, it is convenient to introduce a unit-free radius $\theta = rA$. The constant is given by $A^2 = (4\pi G\rho_c)/K$, where G is the gravitational constant. The radius r_0 is related to the effective temperature T and the central density through $r_0 = \sqrt{\xi_n}/A$, where ξ_n is a fixed appropriate constant for given n so that $r/r_0 = \theta/\sqrt{\xi_n}$. The parameters for the considered density profiles are listed in Table 1. For Bonnor-Ebert spheres the analytical density profiles are only representations of the correct density profile at low and in the limit of high θ . The corresponding constants ξ_n are chosen, as described in Sect. 2.1.1, to match the correct density profiles where the approximations are valid.

The pressure ratio $q^{-1} = p_c/p_{\text{ext}}$ of the central pressure p_c and the external pressure p_{ext} are referred to as ‘overpressure’. As a reference pressure we assume a mean interstellar medium (ISM) pressure $p_{\text{ext}}/k = 2 \times 10^4 \text{ K cm}^{-3}$, as previously suggested by Curry & McKee (2000) based on the study of Boulares & Cox (1990), where the pressure is attributed to thermal, turbulent, and magnetic pressure components. The same value has recently been inferred from the physical parameters and profiles of filaments (Fischera & Martin 2012b,a).

For completeness, we discuss in App. B the PDF of the local density for spheres and cylinders.

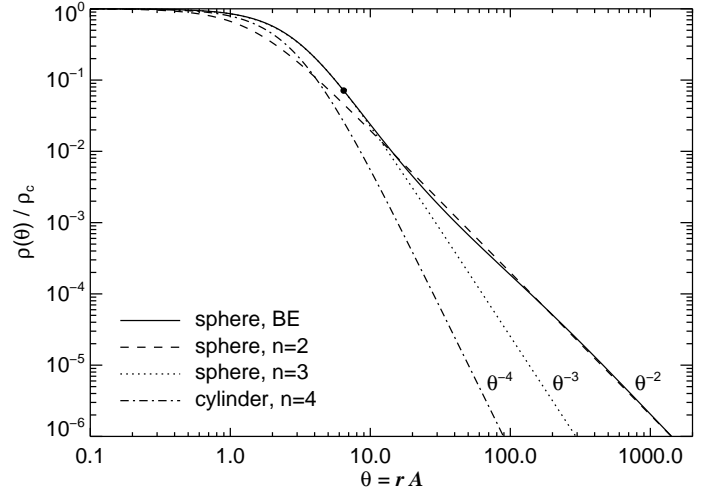


Fig. 1. Normalized radial density profiles of some cases considered in this study given as a function of the unit-free radius $\theta = rA$ where $A^2 = (4\pi G\rho_c)/K$. The filled symbol marks the condition for a critically stable sphere where $\theta_{\text{crit}} \approx 6.451$ and $\rho_c/\rho(\theta_{\text{crit}}) \approx 14.04$. The curves of the analytical density profile given by Eq. 1 are labeled with their asymptotic behavior for $\theta \gg \sqrt{\xi_n}$.

Table 1. Parameters of analytical density profiles

n	isothermal cylinder (exact)	Bonnor-Ebert sphere	
		$\theta < 10$	$\theta \gg 10$
ξ_n	8	3	2
		8.63	2

2.1.1. Bonnor-Ebert sphere

The density profile of an isothermal self-gravitating sphere, or Bonnor-Ebert sphere, is given by

$$\rho(\theta) = \rho_c e^{-\omega(\theta)}, \quad (2)$$

where $\omega = \phi/K$ is the unit-free potential of the gravitational potential ϕ determined by the Lane-Emden equation,

$$\frac{1}{\theta^2} \frac{d}{d\theta} \left[\theta^2 \frac{d\omega}{d\theta} \right] = e^{-\omega}. \quad (3)$$

Spheres have a well-known critically stable configuration with an overpressure above which the sphere becomes gravitationally unstable under compression (Ebert 1955; Bonnor 1956; McCrea 1957; Curry & McKee 2000; Fischera & Dopita 2008; Fischera 2011; Fischera & Martin 2012b) (see App. A.1.1). The critically stable configuration is characterized through an overpressure of $p_c/p_{\text{ext}} \sim 14.04$ at $\theta_{\text{crit}} = 6.451$. However, theoretically, equilibrium solutions with higher overpressures can also be constructed. As in previous papers (Fischera 2011; Fischera & Martin 2012b), we refer to spheres with overpressures below the critical value as subcritical and spheres with higher overpressure as supercritical. The term ‘supercritical’ is often used in the literature to characterize clouds with masses above the critically stable mass. The supercritical spheres in this paper have masses that are *lower* than the mass of a critically stable sphere if we let the temperature and external pressure remain constant, as discussed by Fischera & Martin (2012b) (see also App. A).

As shown in Fig. 1, the profile of the Bonnor-Ebert sphere below $\theta = 10$ or $\rho(r) > \sim 0.01 \rho_c$ is well represented by an analytical density profile as given by Eq. 1 with $n = 3$. For the constant ξ_3 we have chosen a value that is consistent with the overpressure and the size of a critically stable sphere:

$$\xi_3 = \left(\theta_{\text{crit}} q_{\text{crit}}^{1/3} / \sqrt{1 - q_{\text{crit}}^{2/3}} \right)^2 \approx 8.63. \quad (4)$$

This value is used throughout the paper.

At large sizes $\theta \gg 10$ the density profile of the Bonnor-Ebert sphere asymptotically approaches a power-law profile $\rho(\theta)/\rho_c \propto C/\theta^2$ where C is a constant. Inserting the power-law profile in Eq. 3, we find $C = 2$. The same asymptotic behavior is found for an analytical density profile as given in Eq. 1 with $n = 2$ and $\xi_2 = 2$ in the limit of large sizes $z \gg \sqrt{\xi_2}$. We consider this profile as the asymptotic profile of Bonnor-Ebert spheres for high overpressures. Although stable configurations with overpressure above the critical value probably do not exist, the profiles of sub- and supercritical solutions seem to reflect within the observed uncertainties the profiles not only of stable clouds, but also seem to mimic the density profile of collapsing clouds (Kandori et al. 2005; Keto & Caselli 2010; Keto et al. 2014).

Physical parameters of Bonnor-Ebert spheres such as mass and radius are discussed in more detail in App. A in comparison with spheres with a density profile with $n = 3$ or $n = 2$. In App. B.1, we show the variation of the local density PDF with overpressure.

2.1.2. Self-gravitating cylinders

For $n = 4$ the density profile is identical to the profile of an isothermal self-gravitating cylinder with $\xi_4 = 8$ (Stodólkiewicz 1963; Ostriker 1964). The physical parameters of pressurized cylinders have been studied in great detail by Fischera & Martin (2012a). Here, we wish to describe the most important properties for understanding the PDF of the mass surface density of cylinders.

As an important characteristic, a highest possible mass line density $(M/l)_{\text{max}} = 2K/G$ exists for cylinders, which corresponds to a cylinder with infinite overpressure and infinitely small size. As shown in Fischera & Martin (2012a), for example, physical properties such as size, full width at half maximum (*FWHM*), and stability considerations can be expressed through the mass ratio $f_{\text{cyl}} = (M/l)/(M/l)_{\text{max}}$ of the mass line density and the highest possible mass line density. It is related to the pressure ratio q by

$$q = (1 - f_{\text{cyl}})^2. \quad (5)$$

Cylinders with high mass ratio f_{cyl} have a steep density profile $\rho(r) \propto r^{-4}$ at radii $\theta \gg \sqrt{8}$. However, Fig. 1 shows that this asymptotic profile is only established at a relatively large radius $\theta \gg \sim 10$, which approximately corresponds to cylinders with an overpressure $q^{-1} > \sim 100$ or equally to cylinders with mass ratio $f_{\text{cyl}} > \sim 0.9$. Measurements of the density profile of observed filaments in general indicate a flatter density profile more consistent with r^{-2} , as discussed by Fiege & Pudritz (2000), suggesting significantly lower mass ratios. Indications for a filament with a high

mass ratio and a possible steep density profile are found for a filament in the cloud IC 5146 (Fischera & Martin 2012a).¹

2.2. Profile of the mass surface density

The profile of the mass surface density of a pressurized, isothermal, self-gravitating sphere or cylinder seen at inclination angle i is in general given by

$$\Sigma(\theta_{\perp}) = \frac{2}{\cos^{\lambda} i} \sqrt{\frac{1}{q}} \sqrt{\frac{p_{\text{ext}}}{4\pi G}} \int_{\theta_{\perp}}^{\theta_{\text{cl}}} d\theta \frac{\theta_{\perp}}{\sqrt{\theta^2 - \theta_{\perp}^2}} \frac{\rho(\theta)}{\rho_c}, \quad (6)$$

where θ_{\perp} and θ_{cl} are the projected unit-free radius and cloud radius. λ is a power index with $\lambda = 0$ for spheres and $\lambda = 1$ for cylinders. In this convention the inclination angle is $i = 0^\circ$ for a cylinder seen from the side. Profiles for spheres and cylinders for a range of overpressures can be found in the work of Fischera & Martin (2012b). It is noticeable that the profile does not depend on the gas temperature. Consequently, isothermal clouds in a certain pressure region with the same overpressure will have the same profile $\Sigma(\theta)$ independently of their mass or mass line density, which vary for given overpressure with $M_{\text{sph}} \propto T^2/\sqrt{p_{\text{ext}}}$ or $[M/l]_{\text{cyl}} \propto T/\sqrt{p_{\text{ext}}}$ (App. A.1). Their profiles only vary in terms of size as for fixed overpressure $r_{\text{cl}} \propto T/\sqrt{p_{\text{ext}}}$ (App. A.2).

The profiles of the mass surface density for a sphere and a cylinder with a truncated radial density profile as given by Eq. 1 were presented in Paper I. It was found to be convenient to introduce a unit-free mass surface density X_n defined by

$$\Sigma_n = \frac{2}{\cos^{\lambda} i} r_0 \rho_c q^{\frac{n-1}{n}} X_n. \quad (7)$$

The unit-free mass surface density is given by

$$X_n(y_n) = (1 - y_n)^{\frac{1-n}{2}} \int_0^{u_{\text{max}}} du \frac{1}{(1 + u^2)^{n/2}}, \quad (8)$$

where $y_n = (1 - q^{2/n})(1 - x^2)$ and where $x = r_{\perp}/r_{\text{cl}}$ is the ratio of the projected radius r_{\perp} and the cloud radius r_{cl} , which we refer to as the normalized impact parameter. The upper limit of the integral is $u_{\text{max}} = \sqrt{y_n/(1 - y_n)}$. For density profiles with $n = 2, 3$, and 4 the profiles are simple analytical functions and can be found in Paper I.

For isothermal self-gravitating pressurized clouds, we can replace the inner radius using $r_0 = \sqrt{\xi_n}/A$ and the mass surface density becomes

$$\Sigma_n = \frac{2}{\cos^{\lambda} i} \sqrt{\frac{\xi_n p_{\text{ext}}}{4\pi G}} q^{\frac{n-2}{2n}} X_n. \quad (9)$$

We note that for $n = 2$ the relation is independent of the pressure ratio q .

The mass surface density profiles through Bonnor-Ebert spheres is shown in Fig. 2. At small projected radius $\theta_{\perp} \ll 10$ the profile is dominated by the innermost part of the radial density profile and we can use the profile of the analytical density profile with $n = 3$ as approximation. At large

¹ On the other hand, there are claims that star-forming filaments in particular have mass ratios partly considerably higher than the theoretical highest value (Arzoumanian et al. 2011). However, this might be related to the low temperature considered in observational studies (Fischera & Martin 2012b).

projected radius θ_\perp the profile of a Bonnor-Ebert sphere fluctuates asymptotically toward a power law $\Sigma \propto 1/\theta_\perp$. With the exception of small θ_\perp , the mass surface densities of a Bonnor-Ebert sphere is approximately described by a sphere with an analytical density profile with $n = 2$.

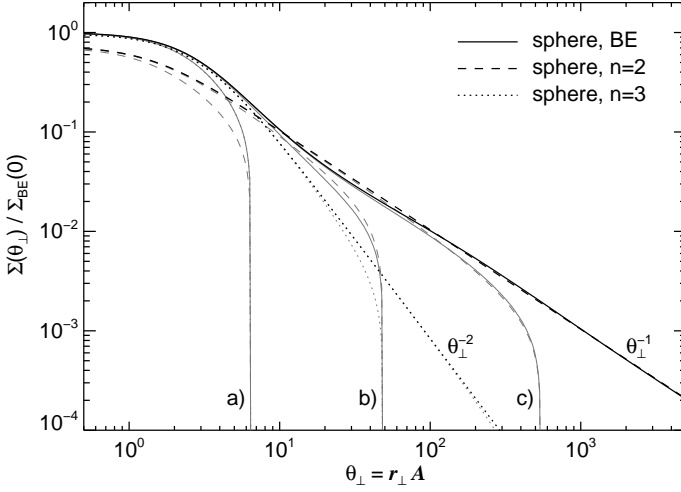


Fig. 2. Profiles of the mass surface density through Bonnor-Ebert spheres and spheres with an analytical density profile as given in Eq. 1. The gray curves are profiles for different cloud radii θ_{cl} . For Bonnor-Ebert spheres the cloud radius corresponds to $q = q_{crit}$ (a), $q = 10^{-2}q_{crit}$ (b), and $q = 10^{-4}q_{crit}$ (c), where $q_{crit} = 1/14.04$. For each assumed cloud radius the central pressure p_c in the considered spheres is the same. The profiles are normalized by the corresponding central mass surface density through a Bonnor-Ebert sphere.

To compare the PDF of Bonnor-Ebert spheres and the PDF of the approximations it is convenient to measure the mass surface density in units of

$$\hat{\Sigma} = 2\sqrt{\frac{p_{ext}}{4\pi G}} = 0.00363\sqrt{\frac{p_{ext}/k}{2 \times 10^4 \text{ K cm}^{-3}}} \text{ g cm}^{-2}. \quad (10)$$

For the truncated analytical density profile with index n the mass surface density becomes

$$\Sigma_n(y_n) = \frac{1}{\cos^\lambda i} \hat{\Sigma} q^{\frac{n-2}{2n}} \sqrt{\xi_n} X_n(y_n). \quad (11)$$

It is common to measure the projected density in visual extinction A_V assuming the optical properties derived for the diffuse interstellar medium. To provide an estimate of the mass surface density in units of extinction A_V we assumed a gas-to-dust ratio of $N_H/E(B-V) = 5.8 \times 10^{21} \text{ cm}^{-2} \text{ mag}^{-1}$ (Bohlin et al. 1978) and an absolute-to-relative extinction R_V of 3.1 (Fitzpatrick 1999) so that

$$A_V/\Sigma = \frac{R_V}{\bar{\mu} m_H} \left(\frac{N_H}{E(B-V)} \right)^{-1} \approx 228 \text{ mag g}^{-1} \text{ cm}^2, \quad (12)$$

where $\bar{\mu} = 1.4$ is the assumed mean atomic gas mass in units of a hydrogen atom with mass m_H .

The critically stable Bonnor-Ebert sphere ($q_{crit} = 1/14.04$) has a normalized central mass surface density of $\Sigma_{crit}(0) \sim 10.0705\hat{\Sigma}$, which corresponds to a central visual extinction of $A_V \sim 8.3 \text{ mag} \sqrt{p_{ext}/k/2 \times 10^4 \text{ K cm}^{-3}}$.

As a special important case we give the behavior of the central mass surface density in the limit of high overpressures. In this regime the central mass surface density through Bonnor-Ebert spheres is approximately given by (Eq. C.4, Fischera & Martin 2012b)

$$\Sigma_{BE}(0) \approx \hat{\Sigma} \frac{1}{\sqrt{q}} 3.028. \quad (13)$$

For spheres and cylinders with analytical density profiles as given in Eq. 1, the upper limit of the integral in Eq. 8 behaves as $u_{max} \rightarrow \infty$ and the central mass surface density becomes approximately

$$\Sigma_n(0) = \frac{1}{\cos^\lambda i} \hat{\Sigma} \sqrt{\frac{\xi_n}{q}} \frac{1}{2} B\left(\frac{n-1}{2}, \frac{1}{2}\right), \quad (14)$$

where

$$B(a, b) = \frac{\Gamma(a)\Gamma(b)}{\Gamma(a+b)} \quad (15)$$

is the beta-function and where $\Gamma(x)$ is the Γ -function. For a sphere with $n = 3$, we obtain with the constant $\xi_3 = 8.63$ in the limit of high overpressures

$$\Sigma_3(0) \approx \hat{\Sigma} \frac{1}{\sqrt{q}} 2.94, \quad (16)$$

which is only 3% lower than the correct asymptotic value of the Bonnor-Ebert sphere.

2.3. Probability distribution function of Bonnor-Ebert spheres

The probability of measuring a mass surface density Σ of an individual sphere in the range from $\Sigma \dots \Sigma + d\Sigma$ is given by

$$P(\Sigma) d\Sigma = P(r_\perp) \left(-\frac{d\Sigma}{dr_\perp} \right)^{-1} d\Sigma, \quad (17)$$

where $P(r_\perp)$ is the probability of measuring a projected radius r_\perp . For a sphere, we have $P(r_\perp) = 2\pi r_\perp / (\pi r_{cl}^2)$.

The derivative of the mass surface density of a cloud with a radial density profile is in general given by

$$\frac{d\Sigma}{dr_\perp}(r_\perp) = 2 \left\{ \int_{r_\perp}^{r_{cl}} dr \frac{d\rho(r)}{dr} \frac{r_\perp}{\sqrt{r^2 - r_\perp^2}} - \frac{r_\perp}{\sqrt{r_{cl}^2 - r_\perp^2}} \rho(r_{cl}) \right\}, \quad (18)$$

where r_{cl} is the cloud radius and r_\perp the projected radius. The integral only applies to the first term in brackets. After substituting the density with $\rho(\theta) = \rho_c e^{-\omega(\theta)}$, we obtain

$$\frac{d\Sigma}{dr_\perp}(\theta_\perp) = -2\rho_c \left\{ \int_{\theta_\perp}^{\theta_{cl}} d\theta e^{-\omega(\theta)} \frac{d\omega}{d\theta} \frac{\theta_\perp}{\sqrt{\theta^2 - \theta_\perp^2}} + \frac{\theta_\perp}{\sqrt{\theta_{cl}^2 - \theta_\perp^2}} e^{-\omega(\theta_{cl})} \right\}, \quad (19)$$

where we have replaced r , r_\perp , and r_{cl} through the corresponding unit-free radii $\theta = rA$, $\theta_\perp = r_\perp A$, and $\theta_{cl} = r_{cl}A$.

with $A = \sqrt{(4\pi G \rho_c)/K}$. Inserting the expression in Eq. 17 provides for the PDF of the Bonnor-Ebert sphere

$$P_{\text{BE}}(\Sigma(\theta_{\perp})) = \sqrt{\frac{4\pi G}{p_{\text{ext}}}} \frac{\sqrt{q}}{\theta_{\text{cl}}^2} \left\{ \int_{\theta_{\perp}}^{\theta_{\text{cl}}} d\theta \frac{e^{-\omega(\theta)}}{\sqrt{\theta^2 - \theta_{\perp}^2}} \frac{d\omega}{d\theta} + \frac{e^{-\omega(\theta_{\text{cl}})}}{\sqrt{\theta_{\text{cl}}^2 - \theta_{\perp}^2}} \right\}^{-1}, \quad (20)$$

where $e^{-\omega(z_{\text{cl}})} = q$, and where we have again replaced the radius and the projected radius by the corresponding unit-free expressions and $K\rho_c$ with p_{ext}/q .

The PDF of Bonnor-Ebert spheres is compared with spheres with an analytical density profile as given in Eq. 1 with $n = 3$ and $n = 2$. The PDF of spheres with such a profile with arbitrary n is given by the implicit function (Paper I)

$$P_{\text{sph}}(\Sigma_n(y_n)) = \left(2r_0\rho_c q^{\frac{n-1}{n}}\right)^{-1} P_{\text{sph}}(X_n(y_n)), \quad (21)$$

where

$$P_{\text{sph}}(X_n(y_n)) = \frac{2}{1 - q^{2/n}} \frac{\sqrt{y_n}(1 - y_n)}{[1 + (n-1)\sqrt{y_n}X_n(y_n)]}. \quad (22)$$

It is straightforward to show that for the approximations of the radial density profile of Bonnor-Ebert spheres the two different expressions 20 and 21 with 22 for the PDF are identical (App. D).

The behavior of the PDF of Bonnor-Ebert spheres with increasing overpressure is shown in Fig. 3. At low overpressures the probabilities are well described by a sphere with an analytical density profile with $n = 3$. The probability for increasing overpressure fluctuates asymptotically toward the value of a sphere with an analytical density profile with $n=2$ in the limit of infinite overpressure.

It is common in observational studies of molecular clouds to measure the logarithmic PDF $P(\ln \Sigma)$ of the mass surface density by estimating the number of mass surface densities Σ within a logarithmic mass surface density bin $\Delta \ln \Sigma$. This is motivated by the large scales in mass surface densities involved, but also by the fact that turbulent cloud structures should show a log-normal density distribution (see Sect. 3.4). As $P(\Sigma) d\Sigma = \Sigma P(\Sigma) d\Sigma/\Sigma = \Sigma P(\Sigma) d \ln \Sigma$ we have $P(\ln \Sigma) = \Sigma P(\Sigma)$. In Paper I, $P(\Sigma)$ is therefore referred to as linear PDF and $\Sigma P(\Sigma)$ as logarithmic PDF of the mass surface density Σ . It follows from Eqs. 6 and 20 that the amplitude of the logarithmic PDF of Bonnor-Ebert spheres is independent of the external pressure. The same is true for clouds with analytical density profiles as $X_n P(X_n) = \Sigma_n P(\Sigma_n)$. The statistical properties of the clouds are thus visualized using the logarithmic PDF.

The PDFs of Bonnor-Ebert spheres for a series of overpressures are shown in Figs. 4 and 5. We might interpret the series of curves as those of an initially stable cloud that becomes gravitationally unstable through cooling or mass accretion and finally collapses.

The PDF shows characteristics discussed in Paper I for spheres with a truncated analytical density profiles as given in Eq. 1, for example, the cutoff at the central mass surface density, the broad maximum above a certain overpressure, and the power-law asymptote in the limit of low mass

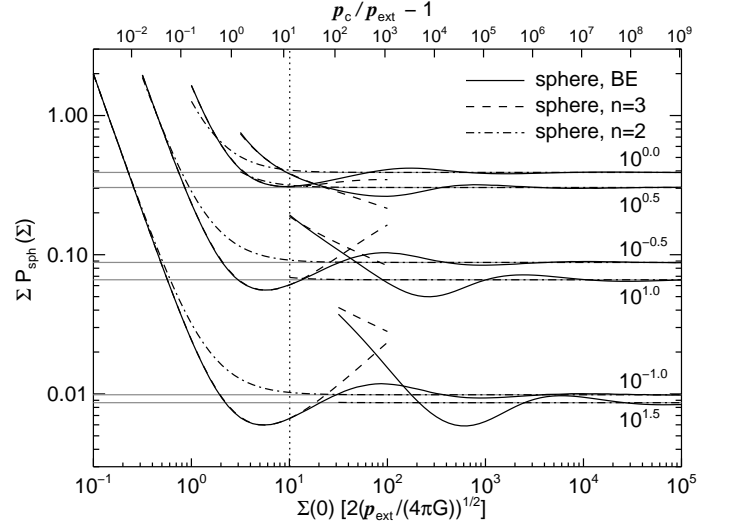


Fig. 3. Probabilities of a number of mass surface densities through Bonnor-Ebert spheres shown as a function of the central mass surface density. The curves are labeled by the corresponding mass surface density given in units of $\hat{\Sigma} = 2\sqrt{p_{\text{ext}}/(4\pi G)}$. The probabilities are compared with those of analytical density profiles as given in Eq. 1 with $n = 3$ and $n = 2$. The probabilities for $n = 3$ are only shown for $\Sigma/\hat{\Sigma} < 100$ where the analytical density profile becomes a valid approximation of the density profile of a Bonnor-Ebert sphere. The overpressures given in the upper axis are only valid for Bonnor-Ebert spheres. The gray lines show the asymptotic probability for Bonnor-Ebert spheres in the limit of infinite overpressure. The vertical dotted line marks the location of the critically stable Bonnor-Ebert sphere.

surface densities where $\Sigma P(\Sigma) \propto \Sigma^2$. For high overpressures, the PDF shows oscillations at high mass surface densities related to the oscillations of the radial density profile (Fig. 1) or the profile of the mass surface densities (Fig. 2). With decreasing mass surface density, the same PDFs fluctuate asymptotically toward the PDF of a sphere with an $n = 2$ -profile. A quantitative analysis of the highest position and the properties at low and high mass surface densities of the PDF of Bonnor-Ebert spheres is given in Sects. 2.3.1, 2.3.2, and 2.3.3.

2.3.1. Maxima position

In this section we quantitatively analyze the highest position of the PDF of Bonnor-Ebert spheres. The normalized impact parameters $[x]_{\text{max}}$ and the mass surface density $[\Sigma]_{\text{max}}$ at the maxima of the linear and logarithmic PDF of Bonnor-Ebert spheres are shown in Fig. 6. The values were derived by solving the conditional equations for maxima positions as given in App. C.

The behavior of the PDF maxima of Bonnor-Ebert spheres are compared with the maxima positions of the corresponding PDFs of spheres with analytical density profiles as given in Eq. 1 with $n=3$ and $n=2$. As found in Paper I, above a certain overpressure the local maxima of the PDF of spheres with analytical density profiles is related to a fixed parameter $[y_n]_{\text{max}}$, and consequently, considering Eq. 8, to a fixed normalized mass surface density $[X_n]_{\text{max}}$. The corresponding values for $n = 2$ and $n = 3$

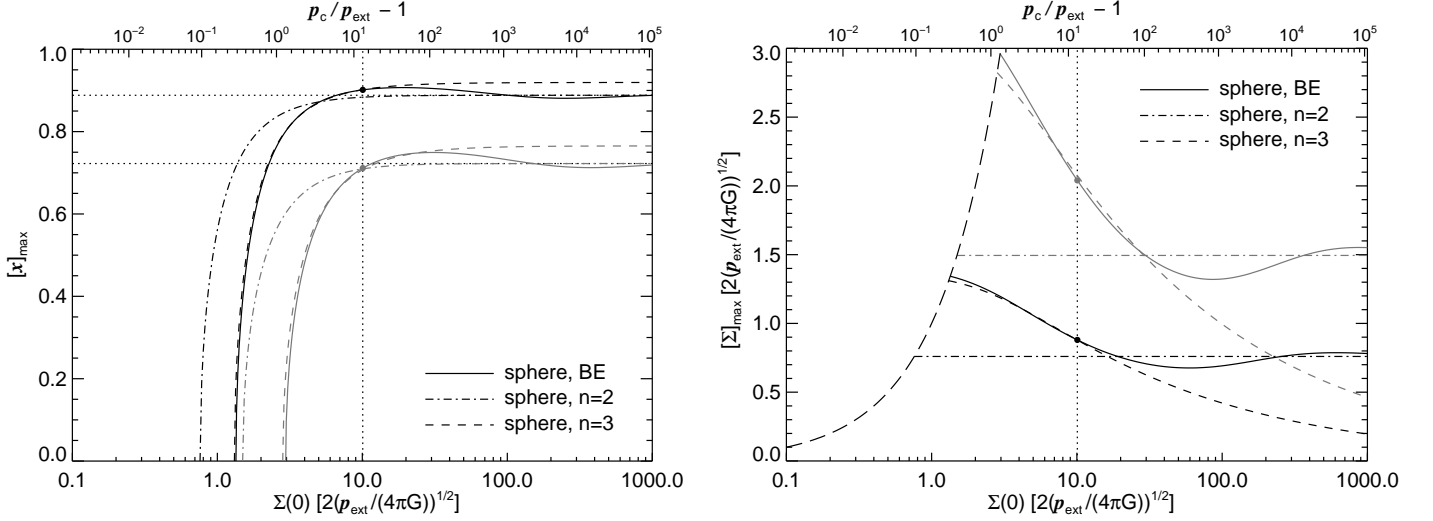


Fig. 6. Normalized impact parameter (left-hand panel) and mass surface density (right-hand panel) at the maximum of the PDF of the mass surface densities of Bonnor-Ebert spheres, given as a function of the central mass surface density. The gray and black curves correspond to the logarithmic and the linear pdf. The values are compared with the corresponding impact parameters and mass surface densities of pressurized spheres with a density profile as given in Eq. 1 with $n = 2$ and $n = 3$. At low central mass surface densities the maximum of the PDF is at impact parameter $[x]_{\max} = 0$ and the curves in the right-hand panel follow the long dashed line where $[\Sigma]_{\max} = \Sigma(0)$. The location of the critically stable Bonnor-Ebert sphere is marked by a vertical dotted line and the corresponding normalized impact parameters and mass surface densities at the PDF maximum as filled circles. The horizontal dotted lines in the left panel are the asymptotic values of the impact parameters of the PDF maximum of Bonnor-Ebert spheres in the limit of high overpressure. The overpressures shown in the upper axis are only valid for the Bonnor-Ebert sphere.

are given in Table 2. The mass surface density $[\Sigma_n]_{\max}$ at the PDF maximum is obtained using the relation given in Eq. 11.

At low overpressures, the maximum coincides in general with the central mass surface density, so that the corresponding impact parameter is $[x]_{\max} = 0$. A local maximum with $[x]_{\max} > 0$ occurs at a sufficiently high overpressure $[q^{-1}]_{0,\max}$. For analytical density profiles the lowest overpressure for a local maximum is given by

$$[q^{-1}]_{0,\max} = (1 - [y_n]_{\max})^{-\frac{n}{2}}. \quad (23)$$

From Eq. 1 we find the corresponding unit-free cloud radius

$$[\theta_{\text{cl}}]_{0,\max} = \sqrt{\xi_n} \sqrt{\frac{[y_n]_{\max}}{1 - [y_n]_{\max}}}. \quad (24)$$

A local maximum with $x > 0$ is otherwise related to a central mass surface density higher than

$$[\Sigma]_{0,\max}/\hat{\Sigma} = (1 - [y_n]_{\max})^{\frac{n-2}{4}} \sqrt{\xi_n} [X_n]_{\max}. \quad (25)$$

Above the lowest overpressure the normalized impact parameter at the PDF maximum of spheres with an analytical density profile behaves as

$$[x]_{\max} = \sqrt{\frac{1 - [y_n]_{\max} - q^{2/n}}{1 - q^{2/n}}}. \quad (26)$$

The impact parameter strongly moves outward with increasing overpressure and asymptotically approaches a constant value at high overpressure given by

$$[x]_{\max} = \sqrt{1 - [y_n]_{\max}}. \quad (27)$$

We see from Fig. 6 that at low overpressure $q^{-1} < 100$, the values of the normalized impact parameter and the mass surface density at PDF maximum of the Bonnor-Ebert sphere follow the values of a sphere with $n = 3$. In this regime, a higher overpressure is related to a lower mass surface density at the PDF maximum. For the logarithmic PDF we find for the maximum

$$[\Sigma_3]_{\max} \approx 0.0075 \sqrt{\frac{p_{\text{ext}}/k}{2 \times 10^4 \text{ K cm}^{-3}}} \left(\frac{q^{-1}}{14.04} \right)^{-\frac{1}{6}} \text{ g cm}^{-2} \quad (28)$$

Assuming diffuse dust properties, this relates to a visual extinction

$$[A_V]_{\max} = 1.72 \sqrt{\frac{p_{\text{ext}}/k}{2 \times 10^4 \text{ K cm}^{-3}}} \left(\frac{q^{-1}}{14.04} \right)^{-\frac{1}{6}} \text{ mag.} \quad (29)$$

At higher overpressure, the impact parameter and the mass surface density at the maximum of the PDF of the Bonnor-Ebert sphere fluctuate asymptotically to the corresponding constant value of a sphere with an analytical density profile with $n=2$. If we consider again the logarithmic PDF, the asymptotic position of the PDF maximum is given by

$$[\Sigma_2]_{\max} = 0.0054 \sqrt{\frac{p_{\text{ext}}/k}{2 \times 10^4 \text{ K cm}^{-3}}} \text{ g cm}^{-2} \quad (30)$$

or

$$[A_V]_{\max} = 1.24 \sqrt{\frac{p_{\text{ext}}/k}{2 \times 10^4 \text{ K cm}^{-3}}} \text{ mag.} \quad (31)$$

Characteristic values of the maxima of the PDF are summarized in Tab. 2. We also add the corresponding values of critically stable conditions both for the Bonnor-Ebert

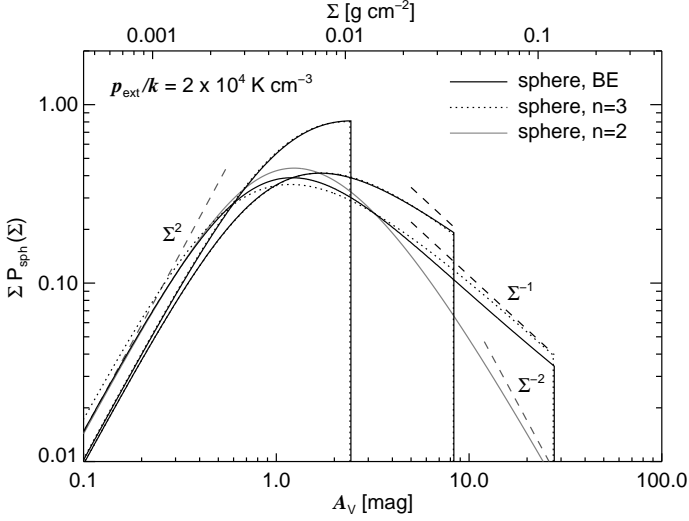


Fig. 4. PDF of the mass surface density of Bonnor-Ebert spheres embedded in a medium with $p_{\text{ext}}/k = 2 \times 10^4 \text{ K cm}^{-3}$ for different gravitational states (solid black curves). The curves correspond to overpressures $q^{-1} = 1 + (q_{\text{crit}}^{-1} - 1) \times 10^i$ with $i = -1, 0, 1$ where $q_{\text{crit}}^{-1} = 14.04$ is the overpressure of a critically stable Bonnor-Ebert sphere. The PDFs are directly compared with those of spheres with a simple density profile (Eq. 1) with $n = 3$ (dotted curves). The black dashed lines are asymptotes of the PDF $\Sigma_3 P_{\text{sph}}(\Sigma_3)$ in the limit of high mass surface densities (Eq. 39). The PDF of a Bonnor-Ebert sphere in the limit of infinite overpressure is shown as a gray curve and is derived assuming a sphere with an analytical density profile with $n = 2$. The gray dashed lines are the corresponding power-law asymptotes in the limit of low (Eq. 34) and high (Eq. 40) mass surface densities.

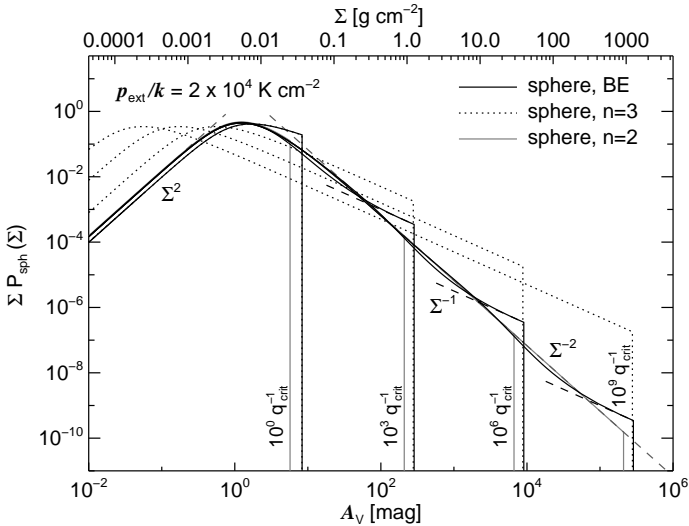


Fig. 5. Similar to Fig. 4, but for a wider range of pressure ratios. We show the transition from a PDF of a critically stable Bonnor-Ebert sphere to the PDFs of highly supercritical spheres. The overpressure is varied in units of the critical value $q_{\text{crit}}^{-1} = 14.04$. Also shown are the corresponding PDFs for a sphere with the analytical density profile with $n = 2$ and $n = 3$. The power-law asymptotes close to the truncation point (black dashed lines) are scaled to the PDF of the Bonnor-Ebert spheres at central mass surface density.

sphere ($q_{\text{crit}}^{-1} = 14.04$) and the sphere with $n=3$ where $q_{\text{crit}}^{-1} = 13.46$ (see Sect. A.1.1). Isothermal self-gravitating pressurized cylinders are known to be stable under compression for all overpressures as $dp(r_{\text{cl}})/dr_{\text{cl}} < 0$ (see Fischera & Martin (2012b) and references therein). The same would apply for a sphere with a hypothetical analytical profile with $n = 2$.

2.3.2. Asymptotic behavior for $\Sigma \ll [\Sigma]_{\text{max}}$

The behavior of the PDF at low mass surface densities is related to the truncation of the density profile and the limit $\Sigma \ll [\Sigma]_{\text{max}}$ is equivalent to $\theta_{\perp} \rightarrow \theta_{\text{cl}}$. In this regime the integrand in Eq. 6 for the mass surface density of Bonnor-Ebert spheres becomes approximately constant with $\rho/\rho_c \approx e^{-\omega(\theta_{\text{cl}})} = q$ and it follows that

$$\Sigma \approx 2\sqrt{q}\sqrt{\frac{p_{\text{ext}}}{4\pi G}}\sqrt{\theta_{\text{cl}}^2 - \theta_{\perp}^2}. \quad (32)$$

Applying Eq. 17 and using $r_{\perp} = \theta_{\perp}/A$, we obtain for the PDF

$$P_{\text{BE}}(\Sigma) \approx \frac{2\pi G}{p_{\text{ext}}} \frac{1}{q\theta_{\text{cl}}^2} \Sigma. \quad (33)$$

The replacement of the unit-free radius with $\theta_{\text{cl}}^2 = r_{\text{cl}}^2 A^2 = \xi_n q^{-\frac{2}{n}} (1 - q^{\frac{2}{n}})$ provides

$$P_{\text{BE}}(\Sigma) \approx \frac{2\pi G}{\xi_n p_{\text{ext}}} \frac{q^{\frac{2-n}{n}}}{1 - q^{2/n}} \Sigma. \quad (34)$$

In the limit of infinite overpressure we obtain with $n = 2$ and $\xi_2 = 2$ the asymptote

$$P_{\text{BE}}(\Sigma) = \frac{\pi G}{p_{\text{ext}}} \Sigma. \quad (35)$$

2.3.3. Asymptotic behavior for $\Sigma \gg [\Sigma]_{\text{max}}$

In Paper I we showed that in the regime of high mass surface densities the PDF of spheres with a truncated radial density profile as given Eq. 1 asymptotically approaches a power law

$$P_{\text{sph}}(X_n) \approx \frac{1}{n-1} \frac{2}{1 - q^{2/n}} X_n^{-\frac{n+1}{n-1}} \zeta_n^{-\frac{2}{n-1}}, \quad (36)$$

where

$$\zeta_n = \frac{1}{2} B\left(\frac{n-1}{2}, \frac{1}{2}\right), \quad (37)$$

where $B(a, b)$ is the beta-function. Using the relation Eq. 9 for the unit-free mass surface density X_n and the relation Eq. 21 provides for the approximations of Bonnor-Ebert spheres the asymptotes

$$P_{\text{sph}}(\Sigma_n) \approx \frac{1}{n-1} \frac{2^{\frac{n+1}{n-1}}}{1 - q^{2/n}} \left(\frac{\xi_n p_{\text{ext}}}{4\pi G}\right)^{\frac{1}{n-1}} \times q^{\frac{n-2}{n(n-1)}} \zeta_n^{\frac{2}{n-1}} \Sigma_n^{-\frac{n+1}{n-1}}. \quad (38)$$

For the logarithmic PDF, the asymptote becomes $\Sigma P(\Sigma) \propto \Sigma^{-\beta}$ with $\beta = 2/(n-1)$. The slope agrees with what is expected for spheres with simple power-law profiles $\rho \propto r^{-n}$ of the local density (Kritsuk et al. 2011; Federrath & Klessen 2013).

Table 2. Location of the PDF maxima

	sphere						cylinder	
	BE	n=3 linear PDF	n=2	BE	n=3 logarithmic PDF	n=2	n=4 lin.	n=4 log.
$[y_n]_{\max}^a$	—	0.155	0.211	—	0.414	0.478	0.141	0.497
$[X_n]_{\max}^a$	—	0.465	0.537	—	1.099	1.057	0.461	1.797
onset for maxima with $[x]_{\max} > 0$								
$[\theta_{\text{cl}}]_{0,\max}$	1.287	1.257	0.731	2.568	2.470	1.353	1.147	2.811
$[\Sigma]_{0,\max}^b$	1.343	1.311	0.760	2.961	2.824	1.494	1.208	3.605
$[q^{-1}]_{0,\max}$	1.291	1.287	1.267	2.319	2.230	1.916	1.356	3.952
critically stable cloud ^c								
$[x]_{\max}$	0.9014	0.9012	—	0.7114	0.7049	—	—	—
$[\Sigma]_{\max}^b$	0.8800	0.8863	—	2.0402	2.0928	—	—	—
maxima in the limit $q \rightarrow 0$								
$[x]_{\max}$	0.888	0.919	0.888	0.722	0.765	0.722	0.927	0.709
$[\Sigma]_{\max}^b$	0.760	0.000	0.760	1.494	0.000	1.494	0.000	0.000

an analytical density profile as given in Eq. 1. The values for cylinders refer to the *asymptotic* PDF without a pole (Eq. 43).

(^c) Critical stability in this paper is defined as critically stable under compression where $dp(r_{\text{cl}})/dr_{\text{cl}} = 0$. (^b) Mass surface density in units of $(2/\cos^\lambda i)\sqrt{p_{\text{ext}}/(4\pi G)}$ with $\lambda = 1$ for cylinders and $\lambda = 0$ for spheres.

We showed (Fig. 2) that the mass surface density at low impact parameters θ_\perp is dominated by the innermost part of the radial density profile of Bonnor-Ebert spheres approximately described by the $n = 3$ -profile, which explains the slope of the asymptote ($\beta = 1$) close to the highest mass surface density. For Bonnor-Ebert spheres with low overpressure we find using Eq. 38

$$P_{\text{BE}}(\Sigma) \approx \frac{2}{1 - q^{2/3}} \sqrt{\frac{\xi_3 p_{\text{ext}}}{4\pi G}} q^{\frac{1}{6}} \Sigma^{-2}. \quad (39)$$

Figure 4 shows that for critically stable spheres the asymptotic behavior is not established. The slope of the logarithmic PDF is more consistent with $\beta = 0.7$ instead of 1. As Fig. 5 shows, Eq. 39 is not applicable for Bonnor-Ebert spheres with high overpressure.

To approximate a Bonnor-Ebert sphere in the limit of high overpressure ($n = 2$, $\xi_2 = 2$, $q \approx 0$) we obtain for the asymptote using Eq. 38

$$P_{\text{BE}}(\Sigma) \approx \frac{\pi p_{\text{ext}}}{G} \Sigma^{-3}. \quad (40)$$

The fluctuation of the PDF at high mass surface densities of Bonnor-Ebert spheres with high overpressure (Fig. 5) are also seen in collapsing-cloud models (Kritsuk et al. 2011). The slope in these simulations is somewhat steeper than for a simple Bonnor-Ebert sphere ($\beta \approx 2.5$), suggesting a flatter density profile ($n \approx 1.8$, for negligible background).

2.4. Probability distribution function of self-gravitating cylinders

The PDF of the mass surface density of cylinders with an analytical density profile as given in Eq. 1 is given by the implicit function (Paper I)

$$P_{\text{cyl}}(\Sigma_n(y_n)) = \left(\frac{2}{\cos i} r_0 \rho_c q^{\frac{n-1}{n}} \right)^{-1} P_{\text{cyl}}(X_n(y_n)), \quad (41)$$

where

$$P_{\text{cyl}}(X_n(y_n)) = \frac{1}{2x} P_{\text{sph}}(X_n(y_n)). \quad (42)$$

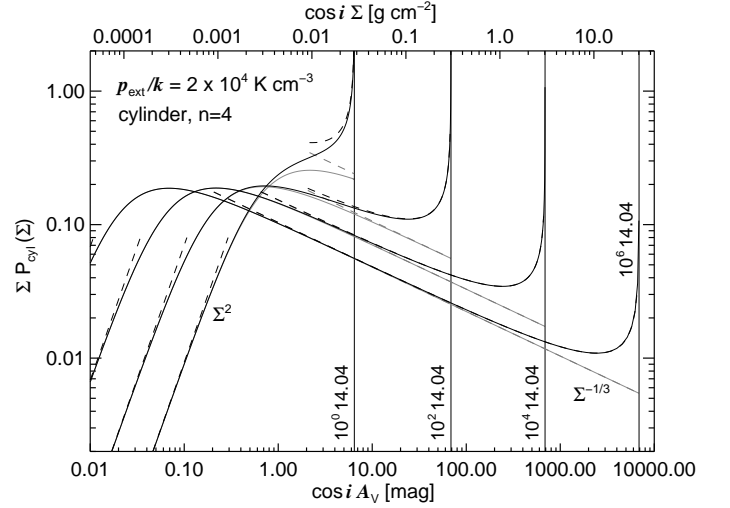


Fig. 7. PDF of the mass surface density of isothermal self-gravitating pressurized cylinders for various overpressures. The vertical line marks the pole position of the PDFs and is labeled with the corresponding pressure ratio q^{-1} . The asymptotes at high and low mass surface density are shown as black dashed lines. The gray curves are the corresponding asymptotic PDFs (Eq. 43) where the pole is removed. The power-law asymptotes at high mass surface densities are shown as gray dashed lines.

$P_{\text{sph}}(X_n)$ is the PDF of spheres of the unit-free mass surface density given by Eq. 22 and x is the normalized impact parameter given by $x = r_\perp/r_{\text{cl}}$.

The PDFs of the mass surface density of isothermal self-gravitating cylinders where $n = 4$ with various pressure ratios are shown in Fig. 7. The pressure ratios and the external pressure are the same as assumed for spheres in Fig. 5. Compared with the PDFs of Bonnor-Ebert spheres, the PDFs of cylinders have a pole at the highest mass surface density. The PDF of cylinder with high overpressure have a local maximum at low mass surface densities that continues to shift to lower mass surface densities for higher overpressures. For the same overpressure the central mass surface density is slightly lower than for spheres (see also

Fischera (2011)). For comparison, the asymptotic PDFs of cylindrical clouds are shown given by (Paper I)

$$P_{\text{cyl}}^{(a)}(\Sigma) = \frac{x}{\sqrt{1-y_n}} P_{\text{cyl}}(\Sigma). \quad (43)$$

Figure 7 shows that the asymptotic PDF provides the correct functional behavior of the cylindrical PDF apart from the pole, which is removed. For example, the asymptotic PDF provides the correct power-law asymptotes at low and high mass surface densities as well as the correct position of the local maximum of the PDF maximum for high overpressures.

2.4.1. Highest position

Because the pole of the PDF of cylinders are close to the highest mass surface density, the analysis of the highest positions of the PDF for isothermal self-gravitating pressurized cylinders have been based upon the asymptotic PDF. Qualitatively, the situation for the asymptotic PDF of cylinders is similar to the PDF of spheres. At low overpressure the local maximum coincides with the central mass surface density. Above a characteristic overpressure the asymptotic PDF develops a local maximum with $[x]_{\text{max}} > 0$, which corresponds to a fixed $[y_n]_{\text{max}}$ and $[X_n]_{\text{max}}$. The values listed in Table 2 for cylinders with an analytical density profile with $n = 4$ are taken from Paper I. The characteristic parameters can be derived as shown for spheres with an analytical density profile.

The impact parameters and the mass surface densities at the local maximum of the asymptotic PDFs with $[x]_{\text{max}} > 0$ are shown in Fig. 8. The normalized impact parameter of the local maximum follows Eq. 26 for $n = 4$. It follows from Eq. 11 that the local maxima $[\Sigma_4]_{\text{max}}$ decrease proportional to $q^{1/4}$ with increasing overpressure. The dependence is slightly stronger than for Bonnor-Ebert spheres with a low overpressure ($q^{-1} < 100$). The local maxima of the logarithmic asymptotic PDF are located at

$$[\Sigma_4]_{\text{max}} = \frac{0.0095}{\cos i} \sqrt{\frac{p_{\text{ext}}/k}{2 \times 10^4 \text{ K cm}^{-3}}} \left(\frac{q}{1/14.04} \right)^{\frac{1}{4}} \text{ mag} \quad (44)$$

or

$$[A_V]_{\text{max}} = \frac{2.17}{\cos i} \sqrt{\frac{p_{\text{ext}}/k}{2 \times 10^4 \text{ K cm}^{-3}}} \left(\frac{q}{1/14.04} \right)^{\frac{1}{4}} \text{ mag}. \quad (45)$$

For low overpressures, the maxima of the asymptotic logarithmic PDFs agree within a factor of two with the maxima of Bonnor-Ebert spheres. Figure 7 shows that at low overpressures the correct PDF of cylinders is still strongly dominated by the pole. In this case, the highest position of the asymptotic PDF approximately corresponds to the location of a shoulder in the correct PDF.

2.4.2. Asymptotic behavior for $\Sigma \ll [\Sigma]_{\text{max}}$

In Paper I, we found for low mass surface densities the asymptote

$$P_{\text{cyl}}(X_n) \approx \frac{1}{1 - q^{2/n}} X_n. \quad (46)$$

For isothermal cylinders we obtain

$$P_{\text{cyl}}(\Sigma) \approx \frac{\cos^2 i}{1 - \sqrt{q}} \frac{\pi G}{\xi_4 p_{\text{ext}}} q^{-1/2} \Sigma. \quad (47)$$

2.4.3. Asymptotic behavior for $\Sigma \gg [\Sigma]_{\text{max}}$

For high overpressure the PDF of a cylinder with the analytical density profile with $n > 1$ behaves at high mass surface densities $\Sigma_n \gg [\Sigma_n]_{\text{max}}$ as (Eq. B.7, Paper I)

$$P_{\text{cyl}}(X_n) \approx \frac{1}{n-1} \frac{1}{\sqrt{1-q^{2/n}}} X_n^{-\frac{n}{n-1}} \zeta_n^{\frac{1}{n-1}} \times \left[1 - \left(\frac{X_n}{X_n(0)} \right)^{\frac{2}{n-1}} \right]^{-\frac{1}{2}}. \quad (48)$$

For self-gravitating isothermal cylinders we obtain using the definition Eq. 7 for X_n and the relation Eq. 41 for the different PDFs for X_n and Σ_n the asymptote

$$P_{\text{cyl}}(\Sigma_4) \approx \frac{1}{3} \frac{1}{\sqrt{1-\sqrt{q}}} \Sigma_4(0)^{\frac{1}{3}} \times \Sigma_4^{-\frac{4}{3}} q^{\frac{1}{3}} \left[1 - \left(\frac{\Sigma_4}{\Sigma_4(0)} \right)^{\frac{2}{3}} \right]^{-\frac{1}{2}}, \quad (49)$$

where

$$\Sigma_4(0) = \frac{\hat{\Sigma}}{\cos i} \sqrt{\frac{\xi_4 \pi}{q}} \quad (50)$$

is the mass surface density through the center of a cylinder in the limit of high overpressure (Eq. 14). For sufficiently high overpressure the PDF shows a power-law slope for $[\Sigma]_{\text{max}} \ll \Sigma \ll \Sigma(0)$ given by

$$P_{\text{cyl}}(\Sigma) \approx \frac{1}{3} \left(\frac{\pi}{2 \cos i} \sqrt{\frac{\xi_4 p_{\text{ext}}}{4 \pi G}} \right)^{1/3} \frac{q^{1/12}}{\sqrt{1-q^{1/2}}} \Sigma^{-4/3}. \quad (51)$$

Figure 7 shows that this power-law behavior is only established for cylinders with overpressures greater than $\sim 10^3$.

3. Averaged probability distribution function

The origin of the observed PDF of the mass surface density of giant molecular clouds is very complex. In general, observations indicate that the global PDF of star-forming molecular clouds is a combination of different components of randomly moving gas, generally attributed to turbulence, and the condensed structures. But structures related to wind-blown bubbles of massive stars or star clusters might also contribute to the global PDF.

The parameters determining the condensed spherical or elongated structures in a molecular cloud are not constant, but show certain variations. The main parameters for the pressurized structures of a certain geometry and density profile (power index n) are the pressure ratio q , the external pressure p_{ext} , and the temperature T_{cl} . The condensed clouds are located on a certain background Σ_b that might also vary for different clouds. The bounding pressure of the condensed structures is probably related to a pressure profile in the larger molecular cloud. Moreover, the condensed structures might form in a hierarchical fashion so that the bounding pressure of the innermost structure is also the central pressure of the surrounding cloud.

Observations (Schneider et al. 2012, 2013) suggest that as a first approach the condensations can be treated as individual structures within the larger molecular cloud. In this

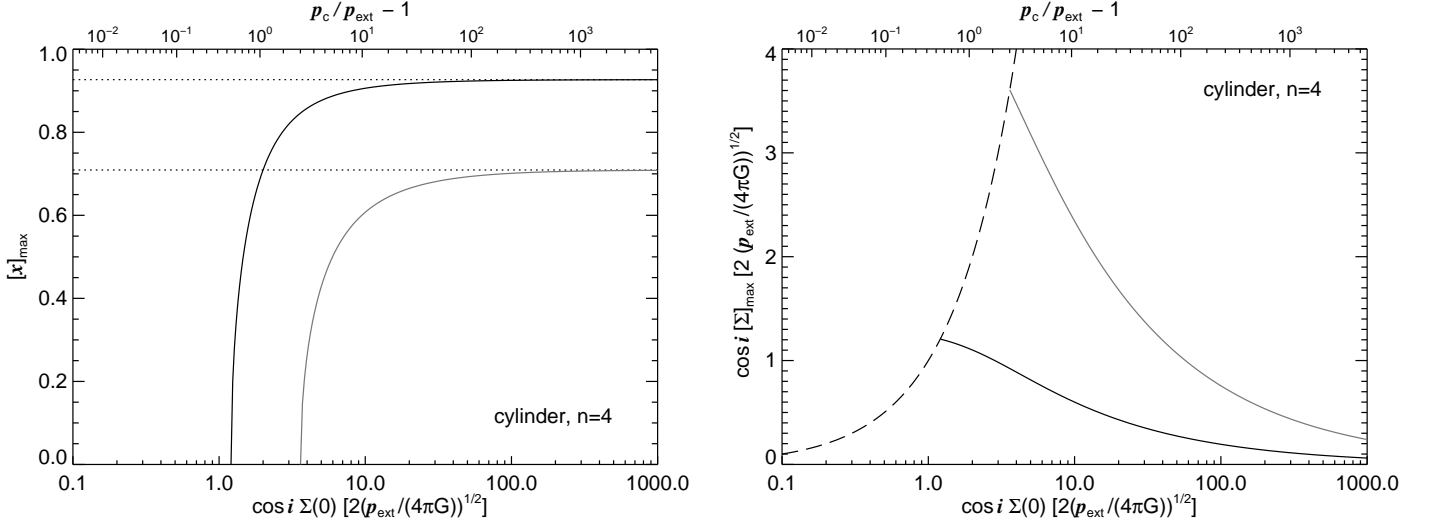


Fig. 8. Same as Fig. 6, but for the asymptotic PDF of isothermal self-gravitating cylinders where the PDF has no pole at the highest mass surface density.

case, we can obtain the mean PDF for the cloud through an average of the PDFs of individual condensations. We furthermore assume that the different parameters determining the individual structures are independent (uncorrelated) variables.

We refer to the PDF of a single condensation under the condition of parameters \mathbf{a} as $P(\Sigma, \mathbf{a})$, where $\mathbf{a} = (q, p_{\text{ext}}, \Sigma_b)$. Under these assumptions, the averaged probability distribution over the distribution functions $P(\mathbf{a})$ is then given by

$$\langle P_{\text{cl}}(\Sigma) \rangle_{\mathbf{a}} = \frac{\int d\mathbf{a} P(\mathbf{a}) r_{\text{cl}}^{\kappa}(\mathbf{a}) P_{\text{cl}}(\Sigma, \mathbf{a})}{\int d\mathbf{a} P(\mathbf{a}) r_{\text{cl}}^{\kappa}(\mathbf{a})}, \quad (52)$$

where $\kappa = 2$ for spheres and $\kappa = 1$ for cylinders.

3.1. Temperature distribution

The mass of a core for a given external pressure and overpressure varies strongly with the kinetic temperature ($M_{\text{sph}} \propto T^2$) (see App. A.1). But as we showed in the previous section, the temperature has no effect on the PDF of the column density if both the external pressure and the overpressure are fixed. All critically stable cores in a certain pressure region, for example, have the same PDF of their mass surface density independent of their temperature. However, because the total size scales with temperature (see App. A.2), the temperature distribution affects the covering factor and therefore the ratio between the PDFs of the cores and the PDF of the surrounding gas.

3.2. Distribution of the gravitational states

In general, the condensed cores in giant molecular clouds are probably in various different gravitational states that are characterized by different pressure ratios q . The situation of the condensed cores might be similar to the situation of Bok globules, which, according to the study of Kandori et al. (2005), show a variety of different pressure ratios q .

To demonstrate the effect of a distribution of the gravitational state on the average PDF of the column den-

sity we consider a large sample of cores that are pressurized by the same external pressure, which is taken to be $p_{\text{ext}}/k = 2 \times 10^4 \text{ K cm}^{-3}$. In addition, we consider the cores to have the same effective temperature and the same K . As shown in App. A.1, the masses of supercritical cores, for example, are smaller than the mass of the critically stable core by up to a factor 2. By fixing p_{ext} and K , the mass of the cores does not vary monotonically with overpressure.

It seems reasonable to assume that the distribution of gravitational states of subcritical and stable spheres ($q^{-1} < q_{\text{crit}}^{-1} \sim 14.04$) follows functional forms different from the distribution of clouds in a supercritical state. As indicated in the study of Bok globules by Kandori et al. (2005), most cores are probably close to the critical value. This might be related to the fact that clouds with a deeper gravitational potential become more stable with a deeper gravitational potential against external disturbances. It might also be a simple observational bias because the central extinction through Bonnor-Ebert spheres strongly increases when the mass approaches the critical value (Fischera & Dopita 2008). The distribution of supercritical states is most likely related to gravitational collapse, as was also considered in the study by Kandori et al. (2005). Because a detailed analysis goes beyond the scope of this paper, we simply assumed that the probability of supercritical states decreases with increasing central density or overpressure q^{-1} .

To be able to consider two different distributions for spheres with low and high overpressure we assume for the probability function of the overpressures the function

$$P(q^{-1}) = C q^{-k_1} \left(1 + (q^{-1}/q_0^{-1})^\gamma \right)^{-\frac{k_1+k_2}{\gamma}}, \quad (53)$$

where $k_2 > 1$. The constant C can be neglected in this study because of the additional renormalization of Eq. 52. The parameter q_0^{-1} is a characteristic overpressure determining the transition between the two regimes. The distribution at $q \gg q_0$ and $q \ll q_0$ are power laws given by $P(q^{-1}) \sim C q^{-k_1}$ and $P(q^{-1}) \sim C (q/q_0)^{k_2} q_0^{-k_1}$. The parameter γ determines the smoothness of the transition between the two power laws. In the limit $\gamma \rightarrow \infty$ the distribution, for example, becomes a broken power law. In this study we assume $\gamma = 2$. For the distribution we assume a

power index $k_1 = 2$, which produces a decreasing probability at lower gravitational states (smaller q^{-1}) for $q^{-1} \ll q_0^{-1}$.

The distribution does not vanish for $q^{-1} \rightarrow 1$, which seems unrealistic. However, the product of the surface area with the probability distribution of the overpressure does indeed vanish as $r_{\text{sph}}(q) \sim r_n(q) \rightarrow 0$ when $q \rightarrow 1$ according to Eq. A.8.

To show the effect of the characteristic overpressure q_0^{-1} we considered two different cases. In a first set of calculations the characteristic overpressure is taken to be the overpressure of a critically stable sphere ($q_0^{-1} = 14.04$). In a second set of calculations the power law of the high q^{-1} -states extends down to lowest gravitational states by choosing $q_0^{-1} \ll 1$. For a direct comparison, the same assumptions were made for both spheres and cylinders. The power index k_2 was varied for given geometry and chosen characteristic overpressure q_0^{-1} to visualize its dependence on the mean PDF. For spheres the assumed power indices k_2 were 1.2, 1.5, and 2.0 and for cylinders 1.5, 2.0, and 3.0.

3.2.1. Mean PDF of spheres

The mean PDFs for distributions of Bonnor-Ebert spheres are shown in Fig. 9. They are compared with the mean PDFs of spheres with analytical density profiles as given in Eq. 1 with $n = 3$.

The mean PDF is characterized by a broad peak at mass surface densities between the highest position of a critically stable sphere and a sphere with infinite overpressure. For the reference pressure the maxima lie at $A_V \sim (1-2)$ mag. At low and high mass surface densities the mean PDF asymptotically approaches the power laws discussed quantitatively in App. E for analytical density profiles.

The power law at low mass surface densities is identical to the power-law asymptote at low mass surface densities of pressurized spheres (Sect. 2.3.2) and cylinders (Sect. 2.4.2) with $\Sigma \langle P_{\text{sph}}(\Sigma) \rangle_q \propto \Sigma^2$. The absolute probabilities follow the probabilities of single highly supercritical Bonnor-Ebert spheres within a factor of two.

The power law at high mass surface densities is independent of the power n of the radial density profile and is given by $\Sigma \langle P_{\text{sph}}(\Sigma) \rangle_q \propto \Sigma^{-2k_2}$. The slope steepens as one would expect for larger k_2 and lower probabilities for spheres with high overpressures. The values of k_2 are limited to $k_2 > 1$. Figure 9 shows that for $k_2 \rightarrow 1$ the mean PDF approaches the PDF of Bonnor-Ebert spheres with infinite overpressure.

The mean PDF for a characteristic pressure ratio $q_0 = 1/14.04$ deviates considerably from the PDF of a critically stable Bonnor-Ebert sphere. At the central mass surface density of a critically stable sphere the mean PDF shows a knee with a flatter curvature at lower and steeper curvature at higher mass surface densities. The feature is more pronounced for higher k_2 . The mean PDF for $q_0 \gg 1$ has no additional feature apart from the prominent peak.

As we see in the figure, for high k_2 and the assumed characteristic pressures q_0 the mean PDF of a distribution of Bonnor-Ebert spheres is well represented by the corresponding mean PDF of a sphere with the analytical density profile with $n = 3$. The two curves only start to deviate for low k_2 where spheres with higher overpressure than $q^{-1} \sim 100$ attribute to the mean PDF where the analyt-

ical density profile with $n = 3$ is not a valid approximation of a Bonnor-Ebert sphere. We have seen that the PDF of an individual sphere with an analytical density profile with $q^{-1} > 100$ is higher than the PDF of a Bonnor-Ebert sphere (Fig. 5) at both low and high mass surface densities. In this case, the mean PDF of the analytical density profile is therefore too high with respect to the correct mean PDF, as seen for $k_2 = 1.2$ and $q_0 = q_{\text{crit}}$.

3.2.2. Mean PDF of cylinders

The mean PDF of an ensemble of self-gravitating isothermal cylinders pressurized by the same external pressure, but with a distribution of pressure ratios q , is shown in Fig. 10. The mean PDF is compared with the PDF of a single cylinder with an overpressure $q^{-1} = 14.04$.

One of the main characteristics is that the mean PDF of a distribution of cylinders has no pole. If we consider the mean PDF for $q_0^{-1} = 14.04$, the PDF has a broad feature located approximately at the pole position of the PDF of a single cylinder with a pressure ratio $q = q_0$. The feature broadens and its maximum shifts to higher mass surface densities for a flatter distribution of q^{-1} or equivalently lower k_2 . The mean PDF for $q_0 \gg 1$, as is also the case for Bonnor-Ebert spheres, has no additional feature apart from the prominent peak at $A_V \sim 1$ mag.

At low and high mass surface densities the mean PDF has power-law asymptotes, similar to the mean PDF of spheres. The asymptotes shown in Fig. 10 are derived in App. E.2. At low mass surface densities the asymptote is again given by $\Sigma \langle P_{\text{cyl}}(\Sigma) \rangle_q \propto \Sigma^2$. At high mass surface densities the slope is flatter than that of a distribution of spheres with $\Sigma \langle P_{\text{cyl}}(\Sigma) \rangle_q \propto \Sigma^{-2k_2+1}$.

3.3. Angle-averaged PDF for cylinders

For filaments, we have the additional complication that the orientation most probably varies not only between different filaments, but may also vary along individual filamentary structures. To analyze its effect on the mean PDF we consider an ensemble of cylinders with a certain distribution of inclination angles i that are otherwise identical (same q).

For randomly distributed filaments, the probability of the cosine of the projection angle i is a constant. However, observations reveal that the orientation of dense massive structures, which probably dominate the PDF, is not completely random. The molecular cloud IC 5146 (Arzoumanian et al. 2011) or the Taurus complex (Kainulainen et al. 2009) are dominated by massive filamentary structures with a certain mean orientation. We ignore the complication that the orientation can change at 90° angles, as is the case for the Taurus filament. To show the effect of any distribution of orientation angles, we assume that the cosine $\mu = \cos i$ of the inclination angle i has a Gaussian distribution $P(\mu)$ around a certain mean μ_0 with a standard deviation σ_μ . The distribution is renormalized so that

$$\int_0^1 d\mu P(\mu) = 1. \quad (54)$$

The limit $\sigma_\mu \gg 1$ produces a flat distribution of randomly orientated cylinders with $P(\mu) = 1$.

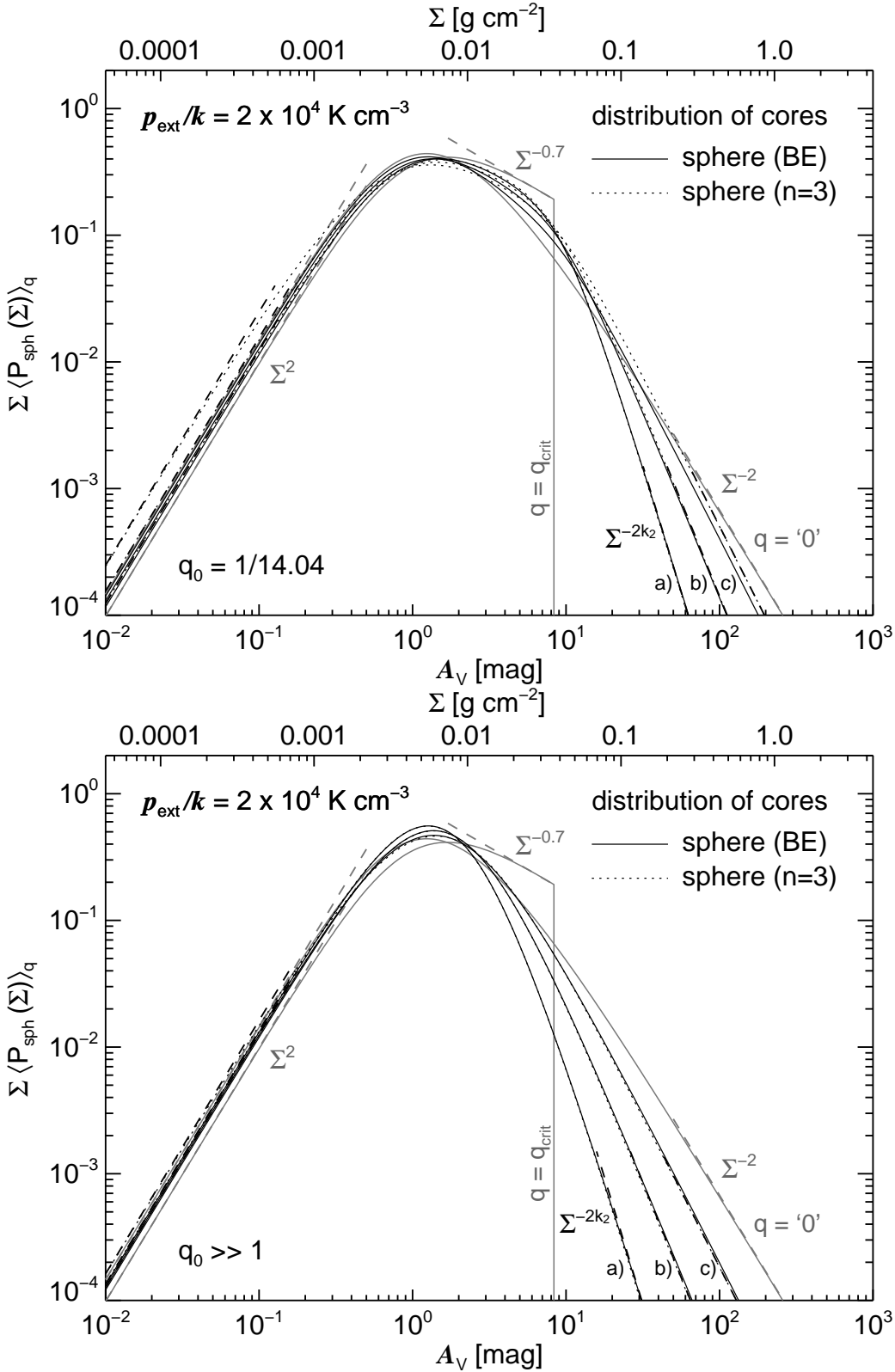


Fig. 9. Mean PDF of the mass surface density for an ensemble of cores assumed to be Bonnor-Ebert spheres with a distribution of gravitational states or pressure ratios q^{-1} as given in Eq. 53. For comparison the mean PDF is also derived for spheres with an analytical density profile as given in Eq. 1 with $n = 3$. The characteristic pressure ratio of the probability distribution of the gravitational states is either $q_0 = q_{\text{crit}} \sim 1/14.04$ of a critically stable sphere (top panel) or $q_0 \gg 1$ (bottom panel). The various curves labeled a), b), and c) correspond to different power indices k_2 assumed to be 2.0, 1.5, and 1.2. The power $k_1 = 2$ and the smoothness parameter $\gamma = 2$ are the same in all calculations. The black dashed lines are power-law approximations of the PDFs in the limit of low and high mass surface densities for an analytical density profile with $n = 3$ (App E.1). The external pressure is assumed to be $p_{\text{ext}}/k = 2 \times 10^4 \text{ K cm}^{-3}$. Also shown are the PDFs of a critically stable sphere and a sphere with infinite overpressure (gray lines and gray annotation). The corresponding power-law asymptotes of the PDFs of single cores in the limit of low (Eq. 34) and high (Eq. 39 and Eq. 40) mass surface densities are shown as gray dashed lines.

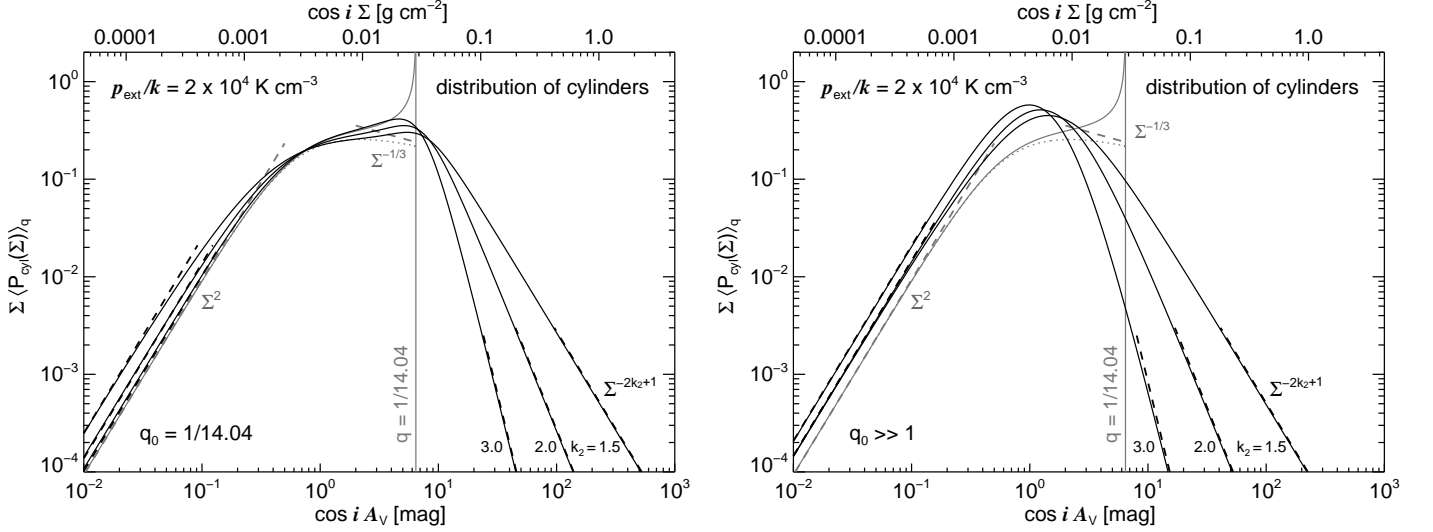


Fig. 10. Mean PDF of the column density for an ensemble of isothermal self-gravitating cylinders with a variety of gravitational states or overpressures q^{-1} , but fixed inclination angle i . The probability distribution of the overpressures is given by Eq. 53 with fixed q_0 , $k_1 = 2$, and $\gamma = 2$ where q_0 is either $1/14.04$ (left-hand figure) or $q_0 \gg 1$ (right-hand figure). The power index k_2 is assumed to be 1.5, 2, and 3. The cylinders are pressurized by a medium with $p_{\text{ext}}/k = 2 \times 10^4 \text{ K cm}^{-3}$. The black dashed lines are asymptotes at low and high mass surface densities (App. E.2). For comparison, the PDF of a single cylinder with overpressure $q^{-1} = 14.04$ is shown (gray line). The gray dotted line is the asymptotic PDF as defined in Eq. 43, and the gray dashed lines are the corresponding asymptotes at low (Eq. 47) and high (Eq. 51) mass surface densities.

If $P_{\text{cyl}}(\Sigma)$ is the PDF for cylinders seen edge-on, the PDF of a cylinder seen at an inclination angle i is given by

$$P'_{\text{cyl}}(\Sigma') = P_{\text{cyl}}(\mu \Sigma') \mu. \quad (55)$$

The average over all inclination angles is then given by

$$\langle P_{\text{cyl}}(\Sigma') \rangle_{\mu} = \int_{\mu_{\min}}^{\mu_{\max}} d\mu P(\mu) P_{\text{cyl}}(\mu \Sigma') \mu, \quad (56)$$

where

$$\mu_{\max} = \begin{cases} \Sigma(0)/\Sigma' & \text{for } \Sigma(0)/\Sigma' < 1, \\ 1 & \text{for } \Sigma(0)/\Sigma' \geq 1, \end{cases} \quad (57)$$

and where μ_{\min} is related to the greatest length of the filament. For infinitely long filaments we have $\mu_{\min} = 0$. The mean PDF for $\Sigma \leq \Sigma(0)$ is an average over all inclination angles. For $\Sigma > \Sigma(0)$ the mean PDF is related to cylinders seen at increasingly high inclination angles.

For randomly distributed cylinders we derive

$$\langle P_{\text{cyl}}(\Sigma') \rangle_{\mu} = \frac{1}{\Sigma'^2} \int_0^{\Sigma'} d\Sigma \Sigma P_{\text{cyl}}(\Sigma). \quad (58)$$

For $\Sigma' > \Sigma(0)$ the angle-averaged PDF of randomly distributed cylinders becomes a simple power law $\langle P_{\text{cyl}}(\Sigma') \rangle_{\mu} = C \Sigma'^{-2}$ where

$$C = \int_0^{\Sigma(0)} d\Sigma \Sigma P_{\text{cyl}}(\Sigma). \quad (59)$$

This power-law slope is the same as for spheres with a density profile with $n = 3$ in the limit of high overpressure (Figs. 4 and 5).

The effect of the angular distribution on the PDF for cylinders is shown in Fig. 11. A distribution of inclination angles reduces the peak at the highest column density and

produces a tail beyond the peak that flattens for wider distributions up to $P_{\text{cyl}}(\Sigma) \propto \Sigma^{-2}$ for randomly oriented cylinders. The effect on the peak is considerably stronger for cylinders with a mean inclination angle $i > 0$ ($\mu_0 < 1$). Figure 11 shows that for $\mu_0 < 1$ the angular distribution also broadens the feature and produces a shift to lower mass surface densities. The PDF of randomly distributed cylinders has a small feature at the central mass surface density for $i = 0$. Because the filamentary structure in the ISM is unlikely to have a well-defined overpressure (p_c/p_{ext}), this feature might be much less prominent than shown in Fig. 11, or might even be absent.

3.4. Background-averaged PDF

In the previous sections we have considered the PDFs of the mass surface density of condensed structures for a negligible background. However, this is certainly no longer valid if the condensed structures are located in molecular clouds or if they are seen through the interstellar medium. As an example, we consider randomly distributed cores in an otherwise turbulent medium. As we show below, the combined PDF of the turbulent structure and the condensed structures resemble the main features of the observed PDF of typical star-forming clouds.

3.4.1. Turbulent medium

As shown in hydrodynamical simulation of driven turbulence, turbulence produces a log-normal density distribution of the local density (Vazquez-Semadeni 1994; Padoan et al. 1997a; Passot & Vázquez-Semadeni 1998).

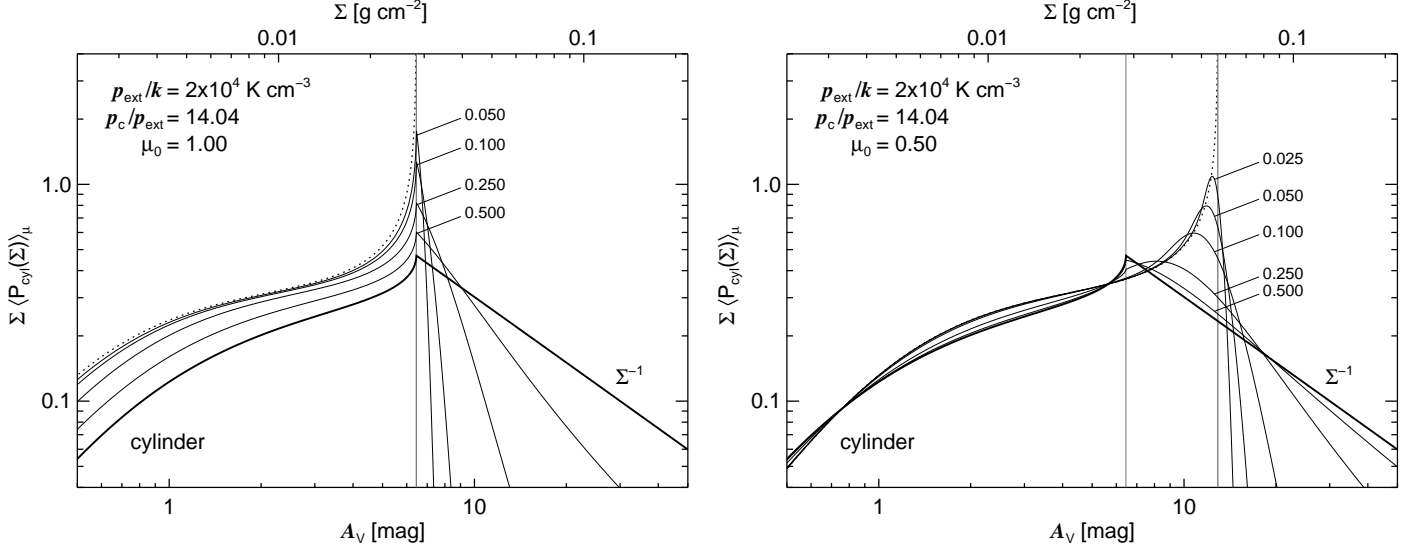


Fig. 11. Angle-averaged PDF of the column density for cylinders with a mean inclination angle of 0° (left-hand figure) and 60° (right-hand figure). The cosine of the inclination angle is assumed to be Gaussian distributed. The curves are labeled with the assumed standard deviation σ_μ . The cylinders are pressurized by a medium with $p_{\text{ext}}/k = 2 \times 10^4 \text{ K cm}^{-3}$ and have an overpressure $p_c/p_{\text{ext}} = 14.04$. The intrinsic PDF for the limit $\sigma_\mu \rightarrow 0$ is shown as dotted curves. The gray vertical lines mark the highest extinction values of a cylinder seen under the assumed inclination angle and the position of the peak of the averaged PDF of randomly oriented cylinders. The thick curves are the PDFs for randomly distributed cylinders.

The log-normal function of a statistical variable s with a mean value $\langle s \rangle$ is given by

$$P(s) = \frac{1}{\sqrt{2\pi} s \sigma_{\ln \hat{s}}} e^{-\frac{1}{2\sigma_{\ln \hat{s}}^2} (\ln \hat{s} + \frac{1}{2}\sigma_{\ln \hat{s}}^2)^2}, \quad (60)$$

where $\hat{s} = s/\langle s \rangle$ is the normalized variable and $\sigma_{\ln \hat{s}}$ the standard deviation of the log-normal function, which is related to the standard deviation of the variable s through

$$\sigma_s^2 = \langle s \rangle^2 (e^{\sigma_{\ln \hat{s}}^2} - 1). \quad (61)$$

According to simulations of driven turbulence (Padoan et al. 1997a; Nordlund & Padoan 1999), there exists a simple linear relation between the standard deviation of the local density and the Mach number M , where

$$\sigma_{\hat{\rho}} = bM. \quad (62)$$

The proportionality factor b and the applicability for the interstellar medium is still a debated question, as discussed in Paper III (Fischera 2014a) or by Kainulainen & Tan (2013). Observational studies of IC 5146 and the Taurus molecular cloud complex suggest a value of $b \sim 0.5$ (Padoan et al. 1997a; Brunt 2010). A lower value ($b \sim 0.20$) has been proposed by Kainulainen & Tan (2013) based on high dynamic-range extinction mapping of infrared dark clouds. Simulations indicate a value between 0.26 and 1 (Padoan et al. 1997b; Passot & Vázquez-Semadeni 1998; Kritsuk et al. 2007; Beetz et al. 2008; Federrath et al. 2008, 2010; Price et al. 2011).

The PDF of the column density through simulated turbulence was also found to be close to a log-normal function (Ostriker et al. 2001; Vázquez-Semadeni & García 2001; Brunt et al. 2010a). The results are supported by studies of the column density through non-star-forming

molecular clouds that agree well with a simple log-normal function, as in the case of Lupus V and the Coalsack (Kainulainen et al. 2009).

The statistical properties of the local density are directly related to the properties of the column density. Their general functional dependence has been described by Fischera & Dopita (2004) and Brunt et al. (2010b,a). Fischera & Dopita (2004) have studied the relationship between the column density and the local density of an isothermal turbulent screen by examining the one- and two-point statistics. They assumed a simple log-normal function of the density distribution of the local density and a simple power law $S(k) = |\hat{\rho}(k)|^2 \propto k^m$ of the power spectrum, where $\hat{\rho}(k)$ is the Fourier coefficient of the local density ρ and k is the wavenumber.

It has been found that if the screen thickness Δ is greater than the highest turbulent scale L_{max} , the variance of the column density of thick screens varies as (Fischera & Dopita 2004)

$$\sigma_{\Sigma/\langle \Sigma \rangle}^2 = \sigma_{\rho/\langle \rho \rangle}^2 \frac{1}{2} \frac{L_{\text{max}}}{\Delta} \frac{[m+3]}{[m+2]} \frac{[1 - (k_{\text{max}}/k_{\text{min}})^{2+m}]}{[1 - (k_{\text{max}}/k_{\text{min}})^{3+m}]}, \quad (63)$$

where $m \neq -2$ and $m \neq -3$. For isolated molecular clouds the thickness should be $\Delta \geq L_{\text{max}}$. Relation 63 allows an estimate of the variance of the local density by measuring both the variance of the column density and the power m of the power spectrum. For a Kolmogorov-like power spectrum of the local density², where $m = -11/3$, and for a wide

² This assumption is correct for a contaminant driven by a Kolmogorov velocity field as might apply to dust particles (Lazarian & Pogosyan 2000; Fischera & Dopita 2004).

range of turbulent length scales ($k_{\max} \gg k_{\min}$), we have, for example,³

$$\sigma_{\Sigma/\langle\Sigma\rangle} = \sigma_{\rho/\langle\rho\rangle} \sqrt{L_{\max}/(5\Delta)}. \quad (64)$$

3.4.2. Combined PDF of cores and turbulent gas

The cores are considered to be small relative to the molecular cloud so that the variations of the column density of the background of individual cores can be neglected. In addition, we consider the simplified case where the cores do not overlap and are homogeneously distributed within the turbulent molecular cloud. The background-averaged PDF of the mass surface density of the cores is then given by the convolution

$$\langle P_{\text{cl}}(\Sigma) \rangle_{\Sigma_b} = \int_0^\Sigma d\Sigma_b P_{\text{cl}}(\Sigma - \Sigma_b) P_{\text{turb}}(\Sigma_b), \quad (65)$$

where $P_{\text{cl}}(\Sigma)$ is the PDF of a single core and $P_{\text{turb}}(\Sigma)$ the PDF of the turbulent medium given by the log-normal function discussed in the previous section. For a narrow distribution of the mass surface density caused by the turbulent medium, the PDF of the background becomes a delta function, and the mean is simply given by

$$\langle P_{\text{cl}}(\Sigma) \rangle_{\Sigma_b} \sim P_{\text{cl}}(\Sigma - \Sigma_b). \quad (66)$$

The cores are assumed to cover a certain fraction f_A of the area of the cloud. The total PDF of the molecular cloud is then given by the combined PDF of the turbulent background and the background-averaged PDF of the cores, so that

$$P_{\text{MC}}(\Sigma) = (1 - f_A) P_{\text{turb}}(\Sigma) + f_A \langle P_{\text{cl}}(\Sigma) \rangle_{\Sigma_b}. \quad (67)$$

Examples of the combined PDF of cores and the turbulent medium are shown in Fig. 12 for two different gravitational states of the cores and three different assumptions of the turbulent medium. The cores are either critically stable or highly supercritical Bonnor-Ebert spheres to mimic collapsing cores. The density profiles are approximated using the corresponding analytical density profiles for low ($n = 3$) and high ($n = 2$) overpressure. The pressure within the turbulent medium is again assumed to be $p_{\text{ext}}/k = 2 \times 10^4 \text{ K cm}^{-3}$. The mean background of the turbulent gas is related to the central mass surface density of a critically stable Bonnor-Ebert sphere. The ratios $\langle \Sigma_b \rangle / \Sigma(0)$ for the mean backgrounds $\langle \Sigma_b \rangle$ and central mass surface density $\Sigma(0)$ through a critically stable sphere are $10^{-1.0}$, $10^{-0.5}$, and $10^{0.0}$ to cover the range from a low to a very high background level. The lowest background is close to the peak position for a number of PDFs of molecular clouds studied by Kainulainen et al. (2009).

To assign a standard deviation of the mass surface density to the different mean backgrounds we considered an idealized turbulent slab with a clearly defined mean density $\langle \rho \rangle$ and a fixed greatest turbulent length scale L_{\max} so that $\sigma_{\Sigma/\langle\Sigma\rangle}^2 \propto 1/\langle\Sigma\rangle$. With Eq. 63, a higher mean background is then related to a lower fluctuation of the normalized mass surface densities $\Sigma/\langle\Sigma\rangle$. As a typical standard deviation we assumed for the lowest mean

background $\sigma_{\Sigma/\langle\Sigma\rangle} = 0.40$ (Table 1, Kainulainen et al. (2009)), which provides a standard deviation of 0.22 and 0.13 for the next higher backgrounds. This implies, considering Eq. 64, a standard deviation of the local density of $\sigma_{\rho/\langle\rho\rangle} = 0.89 \sqrt{\Delta/L_{\max}}$. Assuming for the correlation constant $b = 0.5$ between $\sigma_{\rho/\langle\rho\rangle}$ and M , this suggests a Mach number of $M = 1.8 \sqrt{\Delta/L_{\max}}$. According to Kainulainen & Tan (2013), molecular clouds typically have a Mach number of about $M \sim 10$, which would imply $\Delta \gg L_{\max}$, or, considering a thickness $\Delta \approx L_{\max}$, a smaller correlation coefficient or possibly a flatter power spectrum.

The combined PDF resembles several features of the global PDF of star-forming molecular clouds. The PDF is characterized by a broad peak and a tail at high mass surface densities. The mean PDF of critically stable cores embedded in the turbulent medium is furthermore characterized by a strong decrease of probabilities at high mass surface densities.

The background clearly modifies the shape of the PDF of individual cores. The background-averaged PDF appears squeezed compared with the intrinsic PDF, where the probabilities are shifted to higher mass surface densities that are visible, for example, in the shift of the highest position or in the shift of the knee in the case of critically stable cores. Naturally, the effect on the PDF of the cores increases with background level and is strongest at low mass surface densities.

As discussed in Sect. 2.3.3 and shown in Fig. 12, the high end tail of the PDF of individual cores without background only becomes a power law in the limit of high mass surface densities. However, a low background can reduce the difference between the PDF of the cores and the asymptote and may even produce a tail at high mass surface densities below a possible knee that approximately is a power law. On the other hand, for higher backgrounds with $\langle \Sigma_b \rangle / \Sigma(0) \gg 0.1$, the tail at high mass surface densities develops a curved shape where the probabilities at the low end are considerably higher than the power-law asymptote.

As a result of the additive nature of two different components, the functional form of the mean PDF is not necessarily a simple composition of a turbulent part at low mass surface densities and a tail at high mass surface densities. The appearance will depend on the covering factor and the background level for the condensed cores. Indeed, the theoretical curves of the mean PDFs derived for the high backgrounds show a smooth transition of the log-normal part and a curved tail. For a low background, however, the tail at high mass surface densities shows a broad feature at the low end that is caused by the shifted peak of the background-averaged PDF.

4. Discussion

We have analyzed the PDF of the projected density for several different aspects related to isothermal and self-gravitating structures that are pressurized by the ambient gas. In the following we qualitatively compare the theoretical predictions with the basic properties of observed PDFs of star and non-star-forming molecular cloud as derived by Kainulainen et al. (2009). Paper IV (Fischera 2014b) will present a quantitative analysis of the PDF at low mass surface densities, including the broad maximum referred to

³ Fischera & Dopita (2004) took the power index of the Kolmogorov velocity field to be $m = -10/3$, which leads to $\sigma_{\Sigma/\langle\Sigma\rangle} = \sigma_{\rho/\langle\rho\rangle} \sqrt{L_{\max}/(8\Delta)}$.

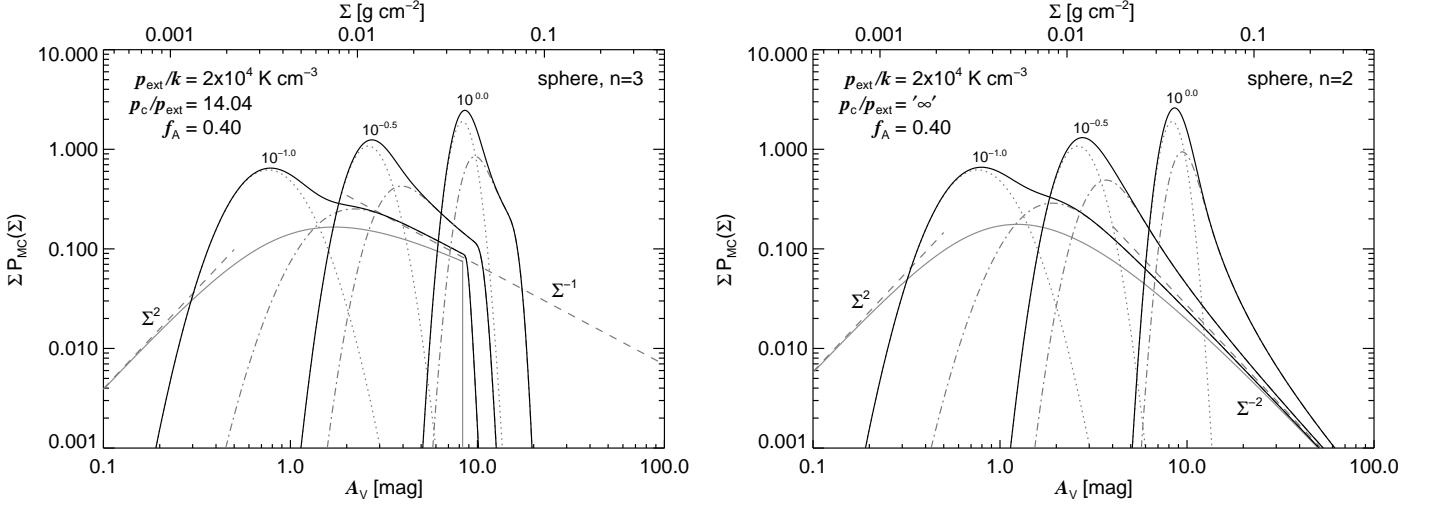


Fig. 12. Combined PDF of a molecular cloud consisting of a turbulent medium (dotted curves) and uniformly distributed condensed cores (dashed-dotted curves). The cores are either critically stable (left) or in a state of collapse (right) where the density profiles are described using the corresponding approximations for Bonnor-Ebert spheres. The turbulent medium is modeled through a simple log-normal function and the pressure in the turbulent gas is assumed to be $p_{\text{ext}}/k = 2 \times 10^4 \text{ K cm}^{-3}$. The spheres do not overlap and cover $f_A = 40\%$ of the area of the molecular cloud. The distributions are labeled with the assumed ratio $\langle \Sigma_b \rangle / \Sigma(0)$ of the mean background $\langle \Sigma_b \rangle$ and the central mass surface density $\Sigma(0)$ through a critically stable Bonnor-Ebert sphere. The scaled intrinsic non-background-averaged PDFs of Bonnor-Ebert spheres (see Fig. 4) are shown as solid gray lines. Also given are the corresponding power-law asymptotes at low (Eq. 34) and at high (Eq. 39 and Eq. 40) mass surface densities.

as the turbulent part and the tail at high mass surface densities.

4.1. High-end tail of the global PDF

The tail at high mass surface densities often has a power-law form. For the PDFs with a maximum at $A_V \sim 1 \text{ mag}$, the index β of the power law approximation $\Sigma^{-\beta}$ of the tail of the logarithmic PDF lies for most cases in between 1 and 2. An unusually steep slope with $\beta > 4$ can be found for the global PDF of the Pipe molecular cloud, which is also characterized by an unusually high maximum position around $A_V \approx 3 \text{ mag}$.

We showed that a distribution of inclination angles of not overlapping cylinders would produce a steep slope at high mass surface densities. The flattest tail with $\beta = 1$ is expected for randomly distributed cylinders. In principle, the slope would be steeper if the filaments had a certain alignment, but this would also be accompanied by a strong feature that is not detected in the observed PDFs. In this case, additional effects need to be considered that might reduce or even remove the feature as a distribution of gravitational states, as shown in this study, or distortions along filaments possibly associated to turbulence, which will be analyzed in Paper III. Still, the tail is expected to show features caused by overlapping filaments that are not accounted for.

We showed that a power-law distribution $P(q^{-1}) \propto 1/(q^{-1})^{k_2}$ of the gravitational states of Bonnor-Ebert spheres or cylinders would lead to a power-law asymptote in the limit of high mass surface densities with $\beta = 2k_2$ for spheres or $\beta = 2k_2 - 1$ for cylinders. A steeper distribution of q^{-1} would be related to a steeper power-law asymptote.

The simplest model for the tail at high mass surface densities are single Bonnor-Ebert spheres. We showed that

spheres with low overpressure $< \sim 100$ have a rather flat asymptote at high mass surface densities with $\beta = 1$ and that the slope above the PDF maximum steepens with overpressure. Clouds with regions essentially in gravitational collapse and in the process of forming new stars are expected to have a tail with a slope close to $\beta = 2$, as observed for the Ophiuchus cloud or Taurus. A flatter tail would be expected for clouds without any star formation activity. In this case, the tail is expected to have a knee or a break at high mass surface densities. These characteristics can be found in the tail of the PDF derived for the Musca molecular cloud, which is classified as non-star-forming. However, the agreement may be coincidental, considering its elongated structure.

A break can also be observed in some other PDFs such as Lupus III, Lupus I, LDN 1228, LDN 204, Ori A, the Perseus cloud, or Ori B. It occurs around $A_V = 6 - 15 \text{ mag}$, which approximately coincides with the central extinction through critically stable spheres pressurized by a medium with $p_{\text{ext}}/k \sim 2 \times 10^4 \text{ K cm}^{-3}$. However, it cannot be excluded that the break may also be caused by the resolution of the map where the high mass surface densities in the central regions of collapsing clouds maybe smoothed over a larger area. These observational problems need to be addressed and can be solved using maps with higher resolution.

The shape of the tail suggests that the condensed structures are seen against a certain background and that the slope of the tail at high mass surface densities steepens with the highest position of the global PDF, as expected for cores that are randomly distributed within a turbulent medium (Sect. 3.4).

We showed that the tail would appear in the case of a low background close to the power law, which is otherwise only expected as an asymptote in the limit of high mass

surface densities. For the PDF of the Taurus complex the power law continues almost down to the highest position without a clear separation of the two components.

The rather steep slope of the PDF tail ($\beta > 4$) of the Pipe molecular cloud might be caused by a rather high background, as suggested by the high maximum position at $A_V \sim 3$ mag. The same may apply to the global PDF of the Rosette molecular cloud. The logarithmic PDF derived by Schneider et al. (2012, 2013) using Herschel observations does not only have a relatively high maximum at $A_V = 2$ mag, but also an unusually steep tail with $\beta \sim 3.1$ (Fig. 6, Schneider et al. (2012)). Relating this slope to a power-law density profile $\rho(r) \propto r^{-n}$ using the relation $n = (2/\beta) + 1$ (Kritsuk et al. 2011; Federrath & Klessen 2013; Fischera 2014) would indicate a rather flat density profile with power $n = 1.65$.⁴ However, the steeper slope may equally well be a direct consequence of condensed structures seen against a relatively high background and not directly related to the density profile.

The PDF of Ophiuchus has a broad peak or a shoulder at the low end of the tail around $A_V \sim 3$ mag, similar to the broad feature in the theoretical mean PDF of condensed cores located on a low background (Fig. 12). The feature at the low end of the PDF tail of the Pipe molecular cloud might have a similar explanation.

4.2. Turbulent part of the global PDF

Most of the derived PDFs of molecular clouds studied by Kainulainen et al. (2009) have a maximum around $A_V = 1$ mag, which is close to the maximum of the PDFs of Bonnor-Ebert spheres pressurized by the assumed ISM pressure. Although it may also be coincidental, this would suggest that the molecular gas as a whole is not only pressurized, but also self-gravitating.

At mass surface densities below the maximum, the observed PDFs show an obvious deviation to a simple log-normal function. For a number of cases the PDF at low mass surface densities has a functional form close to a power law. The deviation may be related to an unsymmetrical nature of the local density PDF, as seen in more current simulations of forced turbulence (Federrath et al. 2008; Konstandin et al. 2012; Federrath & Klessen 2013). The behavior in the limit of low mass surface density might also be related to a truncated density profile of the larger cloud if it is pressurized by a low dense medium. We showed that in the case of a negligible background, the PDF of pressurized nonturbulent spheres and cylinders asymptotically approaches a power law $\Sigma P(\Sigma) \propto \Sigma^2$ at low mass surface densities. The actual shape may be flatter because of the turbulent nature of the gas, even if the PDF of the local density is log-normal, as will be shown in Paper III. It still needs to be considered that the shape in particular at low mass surface densities will be affected by additional material along the line of sight that is not related to the molecular cloud, which will shift the probabilities to higher mass surface densities.

A first estimate of the density fluctuation in the turbulent cloud surrounding the condensed structures can be derived using Eq. 63, which is based on the infinite turbulent

slab approximation. The estimate of the density contrast would be uncertain by the unknown power spectrum of the density structure and the number of turbulent length scale. A statistical analysis of molecular clouds should therefore be combined with studies of the power spectrum of the projected density. A better estimate of the density contrast might be obtained by taking geometric effects and a possible background into account (Papers III and IV).

It appears to be reasonable to assume that most of the star-forming gas lies in the central region of the cloud where the gas is shielded from the interstellar radiation field to allow the gas to cool. The gas also experiences the highest pressure in the center, so that in the case of dynamic equilibrium the gas becomes most easily gravitationally unstable because the critical mass varies as $M_{\text{crit}} \propto T^2/\sqrt{p_{\text{ext}}}$. This would suggest a threshold for star formation as indicated by observational studies (Kirk et al. 2006; Foster et al. 2009). The model described in this paper should allow an independent determination of the central pressure in the turbulent gas and might therefore provide a better understanding of the star formation process.

5. Summary and conclusion

We have analyzed the properties of the PDF of the mass surface density of pressurized isothermal self-gravitating spheres, known as Bonnor-Ebert spheres, and cylinders where we applied the results obtained in Paper I for a simple analytical density profile as a generalization of physical density profiles given by $\rho(r) = \rho_c/(1+(r/r_0)^2)^{n/2}$. We showed that for $\rho(r)/\rho_c > 0.01$ the density profile of Bonnor-Ebert spheres is well approximated by the analytical profile with power $n = 3$. At larger cloud radius the radial density profile fluctuates asymptotically to the analytical profile with $n = 2$. Emphasis was given on the dependence of the PDF of given geometry on the pressure ratio p_{ext}/p_c and the external pressure assumed to be $p_{\text{ext}}/k = 2 \times 10^4 \text{ K cm}^{-3}$.

The main properties of the PDFs of individual spheres and cylinders are found to be as follows:

1. The PDF of critically stable spheres is truncated at the central mass surface density or extinction value $A_V \approx 8.3\sqrt{(p_{\text{ext}}/k)/2 \times 10^4 \text{ K cm}^{-3}} \text{ mag}$.
2. Below an overpressure of ~ 100 , the PDF of a Bonnor-Ebert sphere can be well approximated by the PDF of a sphere with an analytical density profile with $n = 3$. At fixed mass surface density, the PDF of spheres fluctuates asymptotically with overpressure to the value of a sphere with an analytical sphere with $n = 2$ in the limit of infinite overpressure.
3. For the reference pressure the maximum of the logarithmic PDF of a sphere lies between $A_V \sim 1$ mag and 3 mag. For spheres with an overpressure $< \sim 100$, the highest position of the PDF shifts proportionally to $q^{1/6}$ to lower mass surface densities. For highly supercritical clouds the highest position of the logarithmic PDF asymptotically approaches a constant given by $[A_V]_{\text{max}} \sim 1.24\sqrt{(p_{\text{ext}}/k)/2 \times 10^4 \text{ K cm}^{-3}} \text{ mag}$.
4. The flattening of the radial density profile of spheres with overpressure is related to a steepening of the PDF at mass surface densities above the peak maximum. The slope β of the power-law asymptote $\Sigma P_{\text{sph}}(\Sigma) \propto \Sigma^{-\beta}$ varies from $\beta = 1$ for spheres with overpressures below ~ 100 to $\beta = 2$ for highly supercritical spheres.

⁴ The even flatter power law given in the study of Schneider et al. (2012) is inaccurate and has been corrected (Schneider et al. 2013).

5. The highest position of the logarithmic asymptotic PDF (underlying PDF without a pole) of an isothermal self-gravitating pressurized cylinder decreases with $q^{1/4}$. For overpressures below 100, the maxima of cylinders and spheres agree within a factor of two.
6. For cylinders with high overpressure, the PDF at high mass surface densities is approximately given by $P_{\text{cyl}}(\Sigma) \propto \Sigma^{-4/3}(1 - (\Sigma/\Sigma(0))^{2/3})^{-1/2}$.
7. At low mass surface densities the PDF of both spheres and cylinders approaches a power law $P_{\text{cl}}(\Sigma) \propto \Sigma$.

In addition to individual clouds, an ensemble of spheres or cylinders with a distribution of overpressures $q^{-1} = p_c/p_{\text{ext}}$ given by $P(q^{-1}) \propto q^{-k_1}/(1 + (q_0/q)^\gamma)^{\frac{1}{\gamma}(k_1+k_2)}$ were considered. Studied were distributions with fixed parameters $k_1 = 2$ and $\gamma = 2$ and different values for q_0 and k_2 . The corresponding mean PDF has the following properties:

1. The distribution does not change the asymptotic behavior of the PDF at low mass surface density, which is, as in case of individual clouds, proportional to a power law $\langle P(\Sigma) \rangle \propto \Sigma$.
2. At high mass surface densities, the PDF asymptotically approaches a power law that is independent of the radial density profile. This asymptote is either $\langle P_{\text{sph}}(\Sigma) \rangle \propto \Sigma^{-2k_2-1}$ for spheres or $\langle P_{\text{cyl}}(\Sigma) \rangle \propto \Sigma^{-2k_2}$ for cylinders.
3. For cylinders, the distribution effectively decreases the high probabilities at the highest mass surface density of single cylinders.
4. For $q_0 \gg 1$ the mean PDF maximum of spheres and cylinders lies at $A_V = 1 - 2$ mag.

The mean PDF of an ensemble of cylinders with the same overpressure, but a distribution of inclination angles, decreases the high probabilities at the highest mass surface density of single cylinders. Randomly oriented and not overlapping cylinders with a narrow distribution of gravitational states will produce a PDF with a power-law tail $\Sigma P(\Sigma) \propto \Sigma^{-1}$ at high mass surface densities.

A simple model of the global PDF of molecular clouds was presented based on a combination of a turbulent medium and embedded randomly distributed Bonnor-Ebert spheres. The model apparently reproduces the basic features of many of the observed PDFs derived by Kainulainen et al. (2009).

1. The combined model produces a log-normal function around the peak and a tail at high mass surface densities where the relative ratio of the two components is related to the covering factor of the condensed cores.
2. At low covering factor, the combined PDF shows a break between the two components.
3. The functional form of the tail at high mass surface densities is affected by the background level (PDF maximum of the turbulent medium) relative to the PDF maximum of the cores.
 - a) A low background can produce a tail that across the whole range is approximately a power law.
 - b) A high background will lead to a curved tail, where the probabilities at the low end are higher than a power law.

For the assumed reference pressure the background can be considered to be low for $A_V < \sim 1$ mag and high for $A_V > \sim 1$ mag. The curvature for a high background might not be

easily detectable because of limiting resolution and noise in the observed data, so that the assumption of a simple power law would imply a steeper slope than expected for the radial density profile.

References

- Arzoumanian, D., André, P., Didelon, P., et al. 2011, *A&A*, 529, L6
 Beetz, C., Schwarz, C., Dreher, J., & Grauer, R. 2008, *Physics Letters A*, 372, 3037
 Bohlin, R. C., Savage, B. D., & Drake, J. F. 1978, *ApJ*, 224, 132
 Bonnor, W. B. 1956, *MNRAS*, 116, 351
 Boulares, A. & Cox, D. P. 1990, *ApJ*, 365, 544
 Brunt, C. M. 2010, *A&A*, 513, A67
 Brunt, C. M., Federrath, C., & Price, D. J. 2010a, *MNRAS*, 405, L56
 Brunt, C. M., Federrath, C., & Price, D. J. 2010b, *MNRAS*, 403, 1507
 Curry, C. L. & McKee, C. F. 2000, *ApJ*, 528, 734
 Ebert, R. 1955, *Zeitschrift für Astrophysik*, 37, 217
 Federrath, C. & Klessen, R. S. 2013, *ApJ*, 763, 51
 Federrath, C., Klessen, R. S., & Schmidt, W. 2008, *ApJ*, 688, L79
 Federrath, C., Roman-Duval, J., Klessen, R. S., Schmidt, W., & Mac Low, M.-M. 2010, *A&A*, 512, A81
 Federrath, C., Sur, S., Schleicher, D. R. G., Banerjee, R., & Klessen, R. S. 2011, *ApJ*, 731, 62
 Fiege, J. D. & Pudritz, R. E. 2000, *MNRAS*, 311, 85
 Fischera, J. 2011, *A&A*, 526, A33+
 Fischera, J. 2014, *A&A*, 565, A24
 Fischera, J. 2014a, submitted for publication in *A&A*
 Fischera, J. 2014b, submitted for publication in *A&A*
 Fischera, J. & Dopita, M. 2004, *ApJ*, 611, 911
 Fischera, J. & Dopita, M. 2008, *ApJS*, 176, 164
 Fischera, J. & Martin, P. G. 2012a, *A&A*, 547, A86
 Fischera, J. & Martin, P. G. 2012b, *A&A*, 542, A77
 Fitzpatrick, E. L. 1999, *PASP*, 111, 63
 Foster, J. B., Rosolowsky, E. W., Kauffmann, J., et al. 2009, *ApJ*, 696, 298
 Joos & Richter. 1978, *Höhere Mathematik für den Praktiker* (Verlag Harri Deutsch - Thun - Frankfurt)
 Kainulainen, J., Beuther, H., Henning, T., & Plume, R. 2009, *A&A*, 508, L35
 Kainulainen, J. & Tan, J. C. 2013, *A&A*, 549, A53
 Kandori, R., Nakajima, Y., Tamura, M., et al. 2005, *AJ*, 130, 2166
 Keto, E. & Caselli, P. 2010, *MNRAS*, 402, 1625
 Keto, E., Rawlings, J., & Caselli, P. 2014, *MNRAS*, 440, 2616
 Kirk, H., Johnstone, D., & Di Francesco, J. 2006, *ApJ*, 646, 1009
 Konstandin, L., Girichidis, P., Federrath, C., & Klessen, R. S. 2012, *ApJ*, 761, 149
 Kritsuk, A. G., Norman, M. L., Padoan, P., & Wagner, R. 2007, *ApJ*, 665, 416
 Kritsuk, A. G., Norman, M. L., & Wagner, R. 2011, *ApJ*, 727, L20
 Lazarian, A. & Pogosyan, D. 2000, *ApJ*, 537, 720
 McCrea, W. H. 1957, *MNRAS*, 117, 562
 Nordlund, Å. P. & Padoan, P. 1999, in *Interstellar Turbulence*, ed. J. Franco & A. Carramiñana (Cambridge University Press), 218
 Ostriker, E. C., Stone, J. M., & Gammie, C. F. 2001, *ApJ*, 546, 980
 Ostriker, J. 1964, *ApJ*, 140, 1056
 Padoan, P., Jones, B. J. T., & Nordlund, A. P. 1997a, *ApJ*, 474, 730
 Padoan, P., Nordlund, A., & Jones, B. J. T. 1997b, *MNRAS*, 288, 145
 Passot, T. & Vázquez-Semadeni, E. 1998, *Phys. Rev. E*, 58, 4501
 Price, D. J., Federrath, C., & Brunt, C. M. 2011, *ApJ*, 727, L21
 Schneider, N., Csengeri, T., Hennemann, M., et al. 2012, *A&A*, 540, L11
 Schneider, N., Csengeri, T., Hennemann, M., et al. 2013, *A&A*, 551, C1
 Stodólkiewicz, J. S. 1963, *Acta Astronomica*, 13, 30
 Vázquez-Semadeni, E. 1994, *ApJ*, 423, 681
 Vázquez-Semadeni, E. & García, N. 2001, *ApJ*, 557, 727

Acknowledgements. This work was supported by grants from the Natural Sciences and Engineering Research Council of Canada and the Canadian Space Agency. I would like to thank Richard Tuffs for his support and Jouni Kainulainen for helpful discussions. Furthermore, I would like to thank the referee for a careful reading of the manuscript and the suggestions that helped to improve the manuscript. Many thanks go to my parents who enabled me to finish the project.

Appendix A: Approximations of a Bonnor-Ebert sphere

Here, the mass, radius, and mean mass surface density of spheres with an analytical profile given by Eq. 1 are compared with the correct values of Bonnor-Ebert spheres. They are shown in Fig. A.1. Characteristic parameters are listed in Table A.1.

A.1. Mass of Bonnor-Ebert spheres

The mass of a Bonnor-Ebert sphere is given by (Fischera & Dopita 2008)

$$M_{\text{BE}}(\theta_{\text{cl}}) = \frac{K^2}{\sqrt{4\pi G^3 p_{\text{ext}}}} e^{-\omega(\theta_{\text{cl}})/2} \int_0^{\theta_{\text{cl}}} d\theta \theta^2 e^{-\omega(\theta)}, \quad (\text{A.1})$$

where the size θ_{cl} is determined by pressure equilibrium $p_c e^{-\omega(\theta_{\text{cl}})} = p(\theta_{\text{cl}}) = p_{\text{ext}}$.

In Fig. A.1 the mass of Bonnor-Ebert spheres is compared with the masses of spheres using the approximation $n = 3$ and $n = 2$, which are given by

$$M_{\text{sph},3}(q) = \frac{K^2 \xi_3^{3/2} \sqrt{q}}{\sqrt{4\pi G^3 p_{\text{ext}}}} \left\{ \ln \left[q^{-\frac{1}{3}} + q^{-\frac{1}{3}} \sqrt{1 - q^{\frac{2}{3}}} \right] - \sqrt{1 - q^{\frac{2}{3}}} \right\}, \quad (\text{A.2})$$

and

$$M_{\text{sph},2}(q) = \frac{K^2 \xi_2^{3/2} \sqrt{q}}{\sqrt{4\pi G^3 p_{\text{ext}}}} \left\{ \sqrt{\frac{1-q}{q}} - \tan^{-1} \sqrt{\frac{1-q}{q}} \right\}. \quad (\text{A.3})$$

At given external pressure and temperature, the mass of a Bonnor-Ebert sphere increases with increasing overpressure up to the critical value where the sphere has the highest mass. For higher overpressure the mass is lower than the critical value and fluctuates to an asymptotic value at infinite overpressure given by

$$M_{\text{BE}} \rightarrow \frac{\sqrt{8} K^2}{\sqrt{4\pi G^3 p_{\text{ext}}}}. \quad (\text{A.4})$$

A.1.1. Critical stability

Bonnor-Ebert spheres have a well-known critically stable configuration related to the response of the gas pressure at cloud radius in relation to compression. As long as the compression leads to a pressure increase ($dp(r_{\text{cl}})/dr_{\text{cl}} < 0$), a cloud is considered stable, otherwise as unstable. Critical stability is given for

$$\frac{dp(r_{\text{cl}})}{dr_{\text{cl}}} = \frac{dp(r_{\text{cl}})}{dq} \left(\frac{dr_{\text{cl}}}{dq} \right)^{-1} = 0. \quad (\text{A.5})$$

As the derivative of the radius with respect to q is nonzero at the pressure maximum, the critical condition is

$$\frac{dp(r_{\text{cl}})}{dq} = 0. \quad (\text{A.6})$$

For Bonnor-Ebert spheres, a critically stable sphere of the first pressure maximum, which is also the global maximum, is characterized through an overpressure of 14.04.

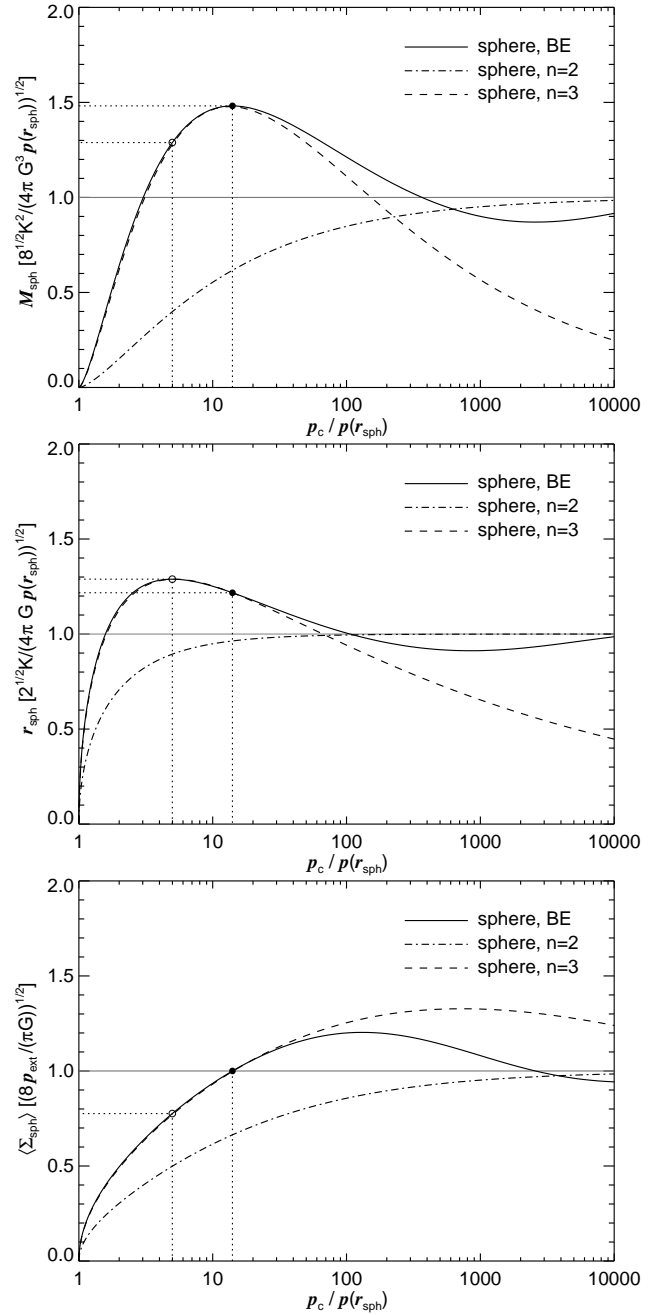


Fig. A.1. Mass, radius, and mean mass surface density of spherical clouds with fixed bounding pressure $p(z_{\text{sph}})$ and temperature as a function of the pressure ratio $p_c/p(z_{\text{sph}})$. The values of a Bonnor-Ebert sphere are compared with the corresponding values of spherical clouds with smooth density profiles as given in Eq. 1 with $n = 2$ and $n = 3$ (dashed-dotted and dashed line, respectively). The dotted vertical and horizontal lines mark the values at maximum radius and at critical stability (filled circle) of Bonnor-Ebert spheres. The mass, radius, and mean mass surface density of a Bonnor-Ebert sphere in the limit of infinite overpressure are shown as gray horizontal lines.

When we apply the same criterion to spheres with an analytical profile as given by Eq. 1 with $n = 3$, we find from Eq. A.2 for fixed mass and fixed K a critical overpressure $q_{\text{crit}}^{-1} = 13.46$, close to the critical value of a Bonnor-Ebert

sphere. The physical parameters corresponding to the critical value of a sphere with $n = 3$ are listed in Table A.1.

As pointed out in the paper of Fischera & Martin (2012b), the critical mass of a Bonnor-Ebert sphere is also the highest possible mass for fixed K and external pressure p_{ext} , but varying pressure ratio q . The same applies for a sphere with $n = 3$. A cylinder, by comparison, has no critical stability with regard to compression. The highest mass line density is related to infinite overpressure. The situation for spheres with a $n = 2$ -profile would be the same as for cylinders.

A.2. Radius of Bonnor-Ebert spheres

The radius of the Bonnor-Ebert sphere is given by

$$r_{\text{BE}}(\theta_{\text{cl}}) = \theta_{\text{cl}} \frac{K}{\sqrt{4\pi G p_{\text{ext}}}} e^{-\omega(z_{\text{cl}})/2}. \quad (\text{A.7})$$

For a cloud with a truncated analytical density profile we find from Eq. 1 and the inner radius $r_0 = \sqrt{\xi_n}/A$, where A can be expressed through $A^2 = 4\pi G p_{\text{ext}}/K^2/q$,

$$r_{\text{cl},n} = \frac{\sqrt{\xi_n} K}{\sqrt{4\pi G p_{\text{ext}}}} q^{1/2-1/n} \sqrt{1 - q^{2/n}}. \quad (\text{A.8})$$

For a given q and p_{ext} the radius increases proportionally to K . Clouds with the same q and K will be smaller in higher pressure regions. Clouds with $n > 2$ have the greatest extension at an overpressure

$$q_{\text{max}}^{-1} = \left(\frac{n}{n-2} \right)^{\frac{n}{2}}. \quad (\text{A.9})$$

Figure A.1 shows that the radius of the Bonnor-Ebert sphere behaves similarly as a function of overpressure as does the mass. However, the cloud with the greatest extension is subcritical with an overpressure of 4.990. The greatest extension of a sphere with $n=3$ corresponds to an overpressure

$$q_{\text{max}}^{-1} = 3^{3/2} \approx 5.196, \quad (\text{A.10})$$

which is close to the highest value of Bonnor-Ebert spheres. For a higher overpressure, the radius of a Bonnor-Ebert sphere is generally smaller than the radius at critical stability, but at a given q it is larger than a sphere with an analytical density profile with $n = 3$. In the limit of high overpressure the radius of the Bonnor-Ebert sphere fluctuates asymptotically toward

$$r_{\text{BE}} \rightarrow \frac{\sqrt{2} K}{\sqrt{4\pi G p_{\text{ext}}}}, \quad (\text{A.11})$$

which is identical with the radius of a sphere with $n = 2$ in the limit of infinite overpressure.

A.3. Mean mass surface density

It has been shown (Fischera & Martin 2012b) that for overpressures where the gas pressure at the cloud boundary of a sphere with fixed mass has local maxima for varying overpressure the mean mass surface density of Bonnor-Ebert spheres is simply given by

$$\langle \Sigma_{\text{BE}} \rangle = \frac{M_{\text{cl}}}{\pi r_{\text{cl}}^2} = \sqrt{\frac{8 p_{\text{ext}}}{\pi G}}. \quad (\text{A.12})$$

The mean value applies, for example, to a critically stable sphere and for a sphere with infinite overpressure (Fig. A.1). For a sphere with infinite overpressure this can be easily verified by replacing the density ratio $e^{-\omega(\theta)}$ by the asymptotic density profile at large scales θ , which is shown in Sect. 2.1.1 to be $2/\theta^2$.

Table A.1. Characteristic cloud parameters

		BE	$n = 3$	$n = 2$
ξ_n			8.63	2
critical mass				
θ_{crit}		6.451	6.340	—
q_{crit}^{-1}		14.04	13.46	—
M_{crit}	$[K^2/\sqrt{4\pi G^3 p_{\text{ext}}}]$	4.191	4.180	—
r_{crit}	$[K/\sqrt{4\pi G p_{\text{ext}}}]$	1.721	1.728	—
$\langle \Sigma \rangle$	$[\sqrt{8 p_{\text{ext}}/(\pi G)}]$	1	0.990	—
$[\Sigma(0)]_{\text{crit}}$	$[\sqrt{p_{\text{ext}}/(\pi G)}]$	10.07	9.778	—
largest radius				
θ_{max}		4.071	4.155	$'\infty'$
q_{max}^{-1}		4.990	$3^{3/2}$	$'\infty'$
M_{sph}	$[K^2/\sqrt{4\pi G^3 p_{\text{ext}}}]$	3.645	3.667	$\sqrt{8}$
r_{max}	$[K/\sqrt{4\pi G p_{\text{ext}}}]$	1.8226	1.8226	$\sqrt{2}$
$\langle \Sigma \rangle$	$[\sqrt{8 p_{\text{ext}}/(\pi G)}]$	0.776	0.781	1
parameters in the limit $\theta \rightarrow \infty, q \rightarrow 0$				
M_{lim}	$[K^2/\sqrt{4\pi G^3 p_{\text{ext}}}]$	$\sqrt{8}$	0	$\sqrt{8}$
r_{lim}	$[K/\sqrt{4\pi G p_{\text{ext}}}]$	$\sqrt{2}$	0	$\sqrt{2}$
$\langle \Sigma \rangle$	$[\sqrt{8 p_{\text{ext}}/(\pi G)}]$	1	0	1

Appendix B: Probability distribution function of the local density

In this section we provide for the sake of completeness the PDF of the local density of spheres and cylinders with a truncated density profile as given by Eq. 1.

The logarithmic PDF is given by

$$\rho P(\rho) = \frac{dV(r)}{dr V_{\text{cl}}} \left(-\frac{1}{\rho} \frac{d\rho}{dr} \right)^{-1}, \quad (\text{B.1})$$

where V_{cl} is the cloud volume and where $V(r)$ is the cloud volume within radius r .

For a truncated density profile with a pressure ratio $p_{\text{ext}}/p_c = q$ we obtain for spheres

$$\rho P_{\text{sph}}(\rho) = \frac{3}{n} \left(\frac{\rho}{\rho(r_{\text{sph}})} \right)^{-\frac{3}{n}} \frac{\sqrt{1 - \left(\frac{\rho}{\rho_c} \right)^{2/n}}}{(1 - q^{2/n})^{3/2}}. \quad (\text{B.2})$$

In the limit of high overpressure this becomes for $(\rho/\rho_c)^{2/n} \ll 1$ a power law

$$\rho P_{\text{sph}}(\rho) \approx \frac{3}{n} \left(\frac{\rho}{\rho(r_{\text{sph}})} \right)^{-\frac{3}{n}}, \quad (\text{B.3})$$

or $\rho P_{\text{sph}}(\rho) \propto \rho^{-3/n}$, as expected for simple radial density profiles $\rho \propto r^{-n}$ (Kritsuk et al. 2011; Federrath et al. 2011).

For cylinders the PDF of the local density is given by

$$\rho P_{\text{cyl}}(\rho) = \frac{2}{n} \frac{1}{1 - q^{2/n}} \left(\frac{\rho}{\rho(r_{\text{cyl}})} \right)^{-\frac{2}{n}}. \quad (\text{B.4})$$

The PDF for a given q over the full range is a power law. For isothermal self-gravitating cylinders we obtain $\rho P_{\text{cyl}}(\rho) \propto \rho^{-\frac{1}{2}}$.

B.1. Local density PDF of Bonnor-Ebert spheres

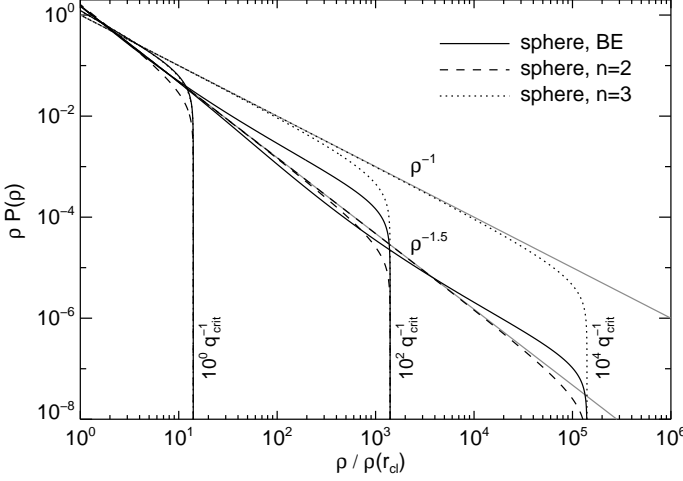


Fig. B.1. Local density PDF of critical and supercritical Bonnor-Ebert spheres for three different pressure ratios, given in units of the overpressure of a critically stable Bonnor-Ebert sphere. They are directly compared with the PDFs of spheres with density profiles as given in Eq. 1 with $n=3$ and $n=2$. Their corresponding power-law asymptotes in the limit of infinite overpressure are shown as gray lines.

Replacing in Eq. B.1 the density by the solution of the Lane-Emden equation $\rho = \rho_c e^{-\omega(\theta)}$ and the radius by the unit-free size $\theta = rA$ provides for the local density PDF of a Bonnor-Ebert sphere

$$\rho P_{\text{BE}}(\rho) = \frac{3\theta^2}{\theta_{\text{cl}}^3} \left(\frac{d\omega}{d\theta} \right)^{-1}. \quad (\text{B.5})$$

The PDFs for critically stable and supercritical Bonnor-Ebert spheres (here defined as a self-gravitating sphere with an overpressure $p_c/p_{\text{ext}} > 14.04$) are shown in Fig. B.1. We showed in Sect. 2.1 that the inner part up to $p_c/p(r) < \sim 100$ of the density profile of self-gravitating spheres can be approximated by an analytical profile as given by Eq. 1 with $n=3$. The shape of the PDF of the Bonnor-Ebert spheres at high density values is consequently determined by this profile. For example, the PDF of Bonnor-Ebert spheres at densities close to the central density value is approximately a power law with ρ^{-1} . For supercritical Bonnor-Ebert spheres, the PDF of density values $\rho \ll \rho_c$ asymptotically approaches the PDF of a sphere with an analytical density profile with $n=2$. The PDF becomes close to a power law $\rho^{-1.5}$.

The values are close to the values obtained with collapse models. Kritsuk et al. (2011) studied the theoretical density distribution in star-forming interstellar clouds. The collapse model provided a PDF that can be approximated over a wide range by a power law $\rho^{-1.695}$. At highest densities the PDF showed a flatter shape approximated by a power law ρ^{-1} and therefore the same as for Bonnor-Ebert

spheres. However, the physical explanation given are rotationally supported cores.

Appendix C: Estimating the maxima of $P_{\text{BE}}(\Sigma)$ and $\Sigma P_{\text{BE}}(\Sigma)$

The maxima positions for linear and logarithmic PDFs of Bonnor-Ebert spheres were derived by estimating the zero points of the first derivatives. The highest positions of the linear and logarithmic PDF fulfill the conditions

$$\frac{d}{d\theta_{\perp}} [P_{\text{BE}}(\Sigma)] = 0, \quad (\text{C.1})$$

$$\frac{d}{d\theta_{\perp}} [\Sigma P_{\text{BE}}(\Sigma)] = 0, \quad (\text{C.2})$$

where the linear PDF of the Bonnor-Ebert sphere is given by

$$P_{\text{BE}}(\Sigma) = \frac{2r_{\perp}}{r_{\text{cl}}^2} \left(-\frac{d\Sigma}{dr_{\perp}} \right)^{-1} = \frac{2\theta_{\perp}}{\theta_{\text{cl}}^2} \left(-\frac{d\Sigma}{d\theta_{\perp}} \right)^{-1}. \quad (\text{C.3})$$

C.1. Linear PDF

Inserting the expression C.3 into the condition Eq. C.1 for the maxima, we obtain

$$\frac{d}{d\theta_{\perp}} [P_{\text{BE}}(\Sigma)] = \frac{2}{\theta_{\text{cl}}^2} \left(\frac{1}{\theta_{\perp}} \frac{d\Sigma}{d\theta_{\perp}} \right)^{-2} \frac{d}{d\theta_{\perp}} \left[\frac{1}{\theta_{\perp}} \frac{d\Sigma}{d\theta_{\perp}} \right] = 0. \quad (\text{C.4})$$

The condition becomes

$$\frac{d}{d\theta_{\perp}} \left[\frac{1}{\theta_{\perp}} \frac{d\Sigma}{d\theta_{\perp}} \right] = 0, \quad (\text{C.5})$$

where the expression in brackets is referred to as $g(\theta_{\perp})$. From the derivative of the mass surface density Eq. 19, it follows that

$$g(\theta_{\perp}) = -2 \frac{\rho_c}{A} \left\{ \frac{e^{-\omega(\theta_{\text{cl}})}}{\sqrt{\theta_{\text{cl}}^2 - \theta_{\perp}^2}} + \int_0^{\sqrt{\theta_{\text{cl}}^2 - \theta_{\perp}^2}} d\theta_{\parallel} \frac{e^{-\omega(\sqrt{\theta_{\parallel}^2 + \theta_{\perp}^2})}}{\sqrt{\theta_{\parallel}^2 + \theta_{\perp}^2}} \frac{d\omega}{d\theta} \bigg|_{\sqrt{\theta_{\parallel}^2 + \theta_{\perp}^2}} \right\}, \quad (\text{C.6})$$

where the integration along the radius θ has been changed to the integration along the depths $\theta_{\parallel} = \sqrt{\theta^2 - \theta_{\perp}^2}$ at impact radius θ_{\perp} . The change of $g(\theta_{\perp})$ by an infinitely small increase $d\theta_{\perp}$ is obtained by expanding the upper limit of the integral and the functions depending on θ_{\perp} into Taylor series. To first order, we find

$$g(\theta_{\perp} + d\theta_{\perp}) = g(\theta_{\perp}) - 2 \frac{\rho_c}{A} d\theta_{\perp} \left\{ \int_0^{\sqrt{\theta_{\text{cl}}^2 - \theta_{\perp}^2}} d\theta_{\parallel} \frac{\theta_{\perp} e^{-\omega(\sqrt{\theta_{\parallel}^2 + \theta_{\perp}^2})}}{\theta_{\parallel}^2 + \theta_{\perp}^2} h(\sqrt{\theta_{\parallel}^2 + \theta_{\perp}^2}) - \frac{e^{-\omega(\theta_{\text{cl}})}}{\sqrt{\theta_{\text{cl}}^2 - \theta_{\perp}^2}} \left[\frac{\theta_{\perp}}{\theta_{\text{cl}}} \frac{d\omega}{d\theta} \bigg|_{\theta_{\text{cl}}} - \frac{\theta_{\perp}}{\theta_{\text{cl}}^2 - \theta_{\perp}^2} \right] \right\}, \quad (\text{C.7})$$

where

$$h(\theta) = \frac{d^2\omega}{d\theta^2}\bigg|_{\theta} - \frac{1}{\theta} \frac{d\omega}{d\theta}\bigg|_{\theta} - \left(\frac{d\omega}{d\theta}\bigg|_{\theta}\right)^2. \quad (\text{C.8})$$

For the derivative we obtain

$$\begin{aligned} \frac{dg(\theta_{\perp})}{d\theta_{\perp}} &= \frac{g(\theta_{\perp} + d\theta_{\perp}) - g(\theta_{\perp})}{d\theta_{\perp}} \\ &= -\frac{2\rho_c}{A} \left\{ \int_{\theta_{\perp}}^{\theta_{\text{cl}}} d\theta \frac{\theta_{\perp} e^{-\omega(\theta)}}{\theta \sqrt{\theta^2 - \theta_{\perp}^2}} h(\theta) - \right. \\ &\quad \left. \frac{e^{-\omega(\theta_{\text{cl}})}}{\sqrt{\theta_{\text{cl}}^2 - \theta_{\perp}^2}} \left[\frac{\theta_{\perp}}{\theta_{\text{cl}}} \frac{d\omega}{d\theta}\bigg|_{\theta_{\text{cl}}} - \frac{\theta_{\perp}}{\theta_{\text{cl}}^2 - \theta_{\perp}^2} \right] \right\}. \quad (\text{C.9}) \end{aligned}$$

C.2. Logarithmic PDF

The condition for the highest positions of the logarithmic PDF is derived in a similar manner. Eq. C.2 provides

$$-\left(\frac{1}{\theta_{\perp}} \frac{d\Sigma}{d\theta_{\perp}}\right)^2 + \frac{\Sigma}{\theta_{\perp}} \frac{d}{d\theta_{\perp}} \left(\frac{1}{\theta_{\perp}} \frac{d\Sigma}{d\theta_{\perp}}\right) = 0. \quad (\text{C.10})$$

Appendix D: Approximation of the $P_{\text{BE}}(\Sigma)$

In this appendix we show for the sake of completeness that for the approximations of Bonnor-Ebert spheres expression 20 of the PDF is identical to Eqs. 21 and 22. Replacing in Eq. 20 the density profile $e^{-\omega(\theta)} = \rho(\theta)/\rho_c$ by the analytical density profile as given in Eq. 1 and the potential by $\omega = -\ln[\rho(\theta)/\rho_c]$, we obtain

$$\begin{aligned} P_{\text{BE}}(\Sigma(\theta_{\perp})) &\sim \sqrt{\frac{4\pi G}{p_{\text{ext}}}} \frac{\sqrt{q}}{\theta_{\text{cl}}^2} \left\{ \frac{q}{\sqrt{\theta_{\text{cl}}^2 - \theta_{\perp}^2}} \right. \\ &\quad \left. + \int_0^{\sqrt{\theta_{\text{cl}}^2 - \theta_{\perp}^2}} d\theta_{\parallel} \frac{n/\xi_n}{(1 + (\theta_{\parallel}^2 + \theta_{\perp}^2)/\xi_n)^{\frac{n}{2}+1}} \right\}^{-1}. \quad (\text{D.1}) \end{aligned}$$

where we have changed the integration along the radius θ to the integration along the depth $\theta_{\parallel} = \sqrt{\theta^2 - \theta_{\perp}^2}$. By introducing the integration variable

$$u = \frac{\theta_{\parallel}/\sqrt{\xi_n}}{\sqrt{1 + \theta_{\perp}^2/\xi_n}} \quad (\text{D.2})$$

and by replacing the projected radius and the cloud radius by $\theta_{\perp} = x\theta_{\text{cl}}$ and $\theta_{\text{cl}} = \sqrt{\xi_n} q^{-1/n} \sqrt{1 - q^{2/n}}$ the expression D.1 can be transformed into

$$\begin{aligned} P_{\text{BE}}(\Sigma(y_n)) &\sim \sqrt{\frac{4\pi G}{\xi_n p_{\text{ext}}}} \frac{q^{\frac{2-n}{2n}}}{1 - q^{2/n}} \left\{ \frac{1}{\sqrt{y_n}} + \right. \\ &\quad \left. \frac{n}{(1 - y_n)^{\frac{1+n}{2}}} \int_0^{u_{\text{max}}} \frac{du}{(1 + u^2)^{\frac{n}{2}+1}} \right\}^{-1}, \quad (\text{D.3}) \end{aligned}$$

where $y_n = (1 - q^{2/n})(1 - x^2)$ and where the upper limit is given by $u_{\text{max}} = \sqrt{y_n/(1 - y_n)}$. The exponent of the

integrand can be reduced by using (simplified version of Eq. 6-57 of Joos & Richter (1978))

$$\int du \frac{1}{(1 + u^2)^m} = \frac{u}{2(m-1)(u^2 + 1)^{m-1}} + \frac{2m-3}{2(m-1)} \int du \frac{1}{(1 + u^2)^{m-1}}, \quad (\text{D.4})$$

which provides

$$\begin{aligned} P_{\text{BE}}(\Sigma(y_n)) &\sim \sqrt{\frac{4\pi G}{\xi_n p_{\text{ext}}}} \frac{q^{\frac{2-n}{2n}}}{1 - q^{2/n}} \left\{ \frac{1}{\sqrt{y_n}(1 - y_n)} + \right. \\ &\quad \left. \frac{n-1}{(1 - y_n)^{\frac{1+n}{2}}} \int_0^{u_{\text{max}}} \frac{du}{(1 + u^2)^{n/2}} \right\}^{-1}. \quad (\text{D.5}) \end{aligned}$$

After applying Eq. 8 for the unit-free mass surface density, we obtain

$$\begin{aligned} P_{\text{BE}}(\Sigma(y_n)) &\sim \sqrt{\frac{4\pi G}{\xi_n p_{\text{ext}}}} \frac{q^{\frac{2-n}{2n}}}{1 - q^{2/n}} \\ &\quad \times \frac{\sqrt{y_n}(1 - y_n)}{[1 + (n-1)\sqrt{y_n}X_n(y_n)]}, \quad (\text{D.6}) \end{aligned}$$

which is identical with Eqs. 21 and 22.

Appendix E: Asymptotes at high and low mass surface densities for q – averaged PDFs

In this appendix we provide the asymptotes at high and low mass surface densities of the mean PDF for a considered distribution of the pressure ratios q of an ensemble of isothermal, self-gravitating, and pressurized spheres or cylinders as shown in Figs. 9 and 10. For the sake of simplicity, for Bonnor-Ebert spheres the analytical approximations for low and high overpressure are considered. The external pressure p_{ext} is considered the same for all clouds in the sample.

For convenience, we introduce the unit-free radius defined by

$$\hat{r}_{\text{cl},n} = \left(\frac{K\sqrt{\xi_n}}{\sqrt{4\pi G p_{\text{ext}}}} \right)^{-1} r_{\text{cl},n} = q^{-\frac{1}{n} + \frac{1}{2}} \sqrt{1 - q^{2/n}}. \quad (\text{E.1})$$

The mean PDF as defined by Eq. 52 at a given mass surface density Σ_n is then given by the integral

$$\langle P_{\text{cl}}(\Sigma_n) \rangle = \frac{1}{\tilde{C}} \int_{q_{\text{min}}^{-1}}^{\infty} dq^{-1} \frac{1}{C} P(q^{-1}) \hat{r}_{\text{cl},n}^{\kappa} P_{\text{cl}}(\Sigma_n, q), \quad (\text{E.2})$$

where $P(q^{-1})$ is the distribution function of the overpressures q^{-1} given by Eq. 53, $P_{\text{cl}}(\Sigma_n, q)$ the conditional PDF under the pressure ratio q , and where \tilde{C} is a normalization constant given by

$$\tilde{C} = \int_1^{\infty} dq^{-1} \frac{1}{C} P(q^{-1}) \hat{r}_{\text{cl},n}^{\kappa}, \quad (\text{E.3})$$

where $\kappa = 2$ for spheres and $\kappa = 1$ for cylinders. The lowest overpressure q_{min}^{-1} is related to the central mass surface density with $\Sigma_n(0) = \Sigma_n$.

E.1. Sphere

E.1.1. Asymptote at high mass surface densities

As shown in Paper I and in Sect. 2.3.3, the PDF of spheres with high overpressure asymptotically approaches within the limit of high mass surface densities the power laws given by Eq. 38. For the product we derive

$$\hat{r}_{\text{cl},n}^2 P_{\text{sph}}(\Sigma_n) \sim \frac{2^{\frac{n+1}{n-1}}}{n-1} \Sigma_n^{-\frac{n+1}{n-1}} \zeta_n^{\frac{2}{n-1}} q^{\frac{n-2}{n-1}} \left(\frac{\xi_n p_{\text{ext}}}{4\pi G} \right)^{\frac{1}{n-1}}. \quad (\text{E.4})$$

Because the probabilities at high mass surface densities are related to spheres with high overpressure (Sect. 2.3), we can simplify the probability distribution Eq. 53 of the overpressure q^{-1} through the corresponding power-law asymptote in the limit $q^{-1} \gg q_0^{-1}$, so that $P(q^{-1}) \sim C q_0^{-k_1-k_2} q^{k_2}$. For the integral E.2 we obtain

$$\begin{aligned} \langle P_{\text{sph}}(\Sigma_n) \rangle &\approx \frac{1}{\tilde{C}} \Sigma_n^{-2k_2-1} \frac{2q_0^{-k_1-k_2}}{(n-1)k_2-1} \\ &\times \left(\frac{\xi_n p_{\text{ext}}}{4\pi G} \right)^{k_2} \text{B} \left(\frac{n-1}{2}, \frac{1}{2} \right)^{2k_2}, \end{aligned} \quad (\text{E.5})$$

where we have replaced the lowest overpressure q_{min}^{-1} by the central mass surface density using Eq. 14.

The estimate of the normalization constant \tilde{C} (Eq. E.3) is straightforward and is

$$\begin{aligned} \tilde{C} = \frac{q_0^{-k_1}}{\gamma} &\left\{ q_0^{-\frac{2}{n}} \text{B}(a, b) \text{I}_\psi(a, b) \right. \\ &\left. - \text{B}(a', b') \text{I}_\psi(a', b') \right\}, \end{aligned} \quad (\text{E.6})$$

where

$$\text{I}_\psi(a, b) = \frac{1}{\text{B}(a, b)} \int_0^\psi dt t^{a-1} (1-t)^{b-1} \quad (\text{E.7})$$

is the normalized incomplete beta-function with $\psi = 1/(1+q_0^\gamma)$ and where

$$a = \frac{k_2 - \frac{2}{n}}{\gamma}, \quad b = \frac{k_1 + \frac{2}{n}}{\gamma}, \quad a' = \frac{k_2}{\gamma}, \quad b' = \frac{k_1}{\gamma}. \quad (\text{E.8})$$

E.1.2. Asymptote at low mass surface densities

In a similar manner as in the previous section, we can derive an asymptote of the mean PDF for low mass surface densities. As discussed in Sect. 2.3.2, the PDF of individual clouds approaches in the limit of low mass surface densities a simple power law given by Eq. 34. We find for the product of the square of the unit-free radius and the PDF the approximation

$$\hat{r}_{\text{cl},n}^2 P_{\text{sph}}(\Sigma_n) \sim \Sigma_n \frac{1}{2} \frac{4\pi G}{\xi_n p_{\text{ext}}}. \quad (\text{E.9})$$

The value does not depend on the overpressure q^{-1} .

In the limit of low mass surface densities we can approximate $q_{\text{min}}^{-1} \approx 1$. The mean asymptotic value of the PDF is then given by

$$\langle P_{\text{sph}}(\Sigma_n) \rangle \sim \frac{1}{\tilde{C}} \Sigma_n \frac{q_0^{-k_1-1}}{2\gamma} \frac{4\pi G}{\xi_n p_{\text{ext}}} \text{B}(a, b) \text{I}_\psi(a, b) \quad (\text{E.10})$$

with $\psi \approx 1/(1+q_0^\gamma)$ and

$$a = \frac{1}{\gamma}(k_2 - 1), \quad b = \frac{1}{\gamma}(k_1 + 1). \quad (\text{E.11})$$

The slope of the asymptotic power law for low mass surface densities is the same as for individual clouds.

E.2. Cylinder

E.2.1. Asymptote at high mass surface densities

To estimate the mean value of the PDF for high mass surface densities we can apply the approximation Eq. 49. For the product of radius and PDF we obtain

$$\begin{aligned} \hat{r}_{\text{cl},4} P(\Sigma_4) &\approx \frac{1}{3} \left(\frac{\pi}{2 \cos i} \right)^{\frac{1}{3}} \left(\frac{\xi_4 p_{\text{ext}}}{4\pi G} \right)^{\frac{1}{6}} \\ &\times \Sigma_4^{-\frac{4}{3}} q^{\frac{1}{3}} \left[1 - (q_{\text{min}}^{-1}/q^{-1})^{\frac{1}{3}} \right]^{-\frac{1}{2}}, \end{aligned} \quad (\text{E.12})$$

where we have replaced the central mass surface density by the asymptotic value given by Eq. 50 valid in the limit of high overpressure. The same replacement has been made for the fixed mass surface density Σ_4 in the denominator, which is related to the lowest overpressure q_{min}^{-1} . To estimate the integral E.2 we can make the same simplification as in App. E.1.1 by replacing the probability distribution Eq. 53 by the corresponding power law $P(q^{-1}) \sim C q_0^{-k_1-k_2} q^{k_2}$. For the mean PDF of self-gravitating cylinders we obtain as the asymptote at high mass surface densities

$$\begin{aligned} \langle P_{\text{cyl}}(\Sigma_4) \rangle &\approx \frac{1}{\tilde{C}} \Sigma_4^{-2k_2} \text{B} \left(3k_2 - 2, \frac{1}{2} \right) q_0^{-k_1-k_2} \\ &\times \left(\frac{\xi_4 p_{\text{ext}}}{4\pi G} \right)^{k_2-\frac{1}{2}} \left(\frac{\pi}{2 \cos i} \right)^{2k_2-1}. \end{aligned} \quad (\text{E.13})$$

To provide a simple analytical estimate for the normalization constant \tilde{C} we can consider the two extreme cases we discussed here. For a distribution in q^{-1} with $q_0^{-1} \gg 1$ the radius can be simplified to $\hat{r}_4 \approx q^{\frac{1}{4}}(1 - 0.5q^{1/2})$. The estimate of the integral E.3 is again straightforward and the normalization constant becomes

$$\begin{aligned} \tilde{C} &\approx \frac{q_0^{-k_1-\frac{3}{4}}}{\gamma} \left\{ \text{B}(a, b) \text{I}_\psi(a, b) \right. \\ &\left. - \frac{q_0^{\frac{1}{2}}}{2} \text{B}(a', b') \text{I}_\psi(a', b') \right\}, \end{aligned} \quad (\text{E.14})$$

where

$$a = \frac{k_2 - \frac{3}{4}}{\gamma}, \quad b = \frac{k_1 + \frac{3}{4}}{\gamma}, \quad a' = \frac{k_2 - \frac{1}{4}}{\gamma}, \quad b' = \frac{k_1 + \frac{1}{4}}{\gamma}. \quad (\text{E.15})$$

For $q_0^{-1} \ll 1$, the distribution of overpressure is a simple power law $P(q^{-1}) \sim C q_0^{-k_1-k_2} q^{k_2}$ and the integral can be solved without further simplification. The normalization constant becomes

$$\tilde{C} = 2q_0^{-k_1-k_2} \text{B} \left(2k_2 - \frac{3}{2}, \frac{3}{2} \right). \quad (\text{E.16})$$

E.2.2. Asymptote at low mass surface densities

In the limit of low mass surface densities it follows from Eqs. 34 and 41 with 42 that the asymptote of the PDF in the limit of low mass surface densities is given by

$$P_{\text{cyl}}(\Sigma_4) \approx \frac{1}{1 - q^{1/2}} \frac{\pi G}{\xi_4 p_{\text{ext}}} \frac{1}{x} q^{-\frac{1}{2}} \Sigma_4. \quad (\text{E.17})$$

For low mass surface densities the mean PDF is dominated by $x \approx 1$. For the product of radius and PDF we obtain

$$\hat{r}_{\text{cl},4} P_{\text{cyl}}(\Sigma_4) \approx \frac{\pi G}{\xi_4 p_{\text{ext}}} \Sigma_4 q^{-\frac{1}{4}} \frac{1}{\sqrt{1 - q^{1/2}}}. \quad (\text{E.18})$$

For large $q_0^{-1} \gg 1$ the contribution to the mean PDF is related to high overpressures so that we can simplify the expression by removing the square root using $1/\sqrt{1 - q^{1/2}} \approx 1 + 0.5 q^{1/2}$. The asymptote of the mean PDF at low mass surface densities becomes

$$\begin{aligned} \langle P_{\text{cyl}}(\Sigma_4) \rangle \approx & \frac{1}{\tilde{C}} \Sigma_4 \frac{\pi G}{\xi_4 p_{\text{ext}}} \frac{q^{-k_1 - \frac{5}{4}}}{\gamma} \left\{ \text{B}(a, b) \text{I}_\psi(a, b) \right. \\ & \left. + \frac{q^{\frac{1}{2}}}{2} \text{B}(a', b') \text{I}_\psi(a', b') \right\}, \end{aligned} \quad (\text{E.19})$$

where

$$a = \frac{k_2 - \frac{5}{4}}{\gamma}, \quad b = \frac{k_1 + \frac{5}{4}}{\gamma}, \quad a' = \frac{k_2 - \frac{3}{4}}{\gamma}, \quad b' = \frac{k_1 + \frac{3}{4}}{\gamma}. \quad (\text{E.20})$$

For the limit $q_0^{-1} \ll 1$, where the probability distribution $P(q^{-1})$ becomes a simple power law, we find

$$\langle P_{\text{cyl}}(\Sigma_4) \rangle \approx \frac{1}{\tilde{C}} \Sigma_4 \frac{\pi G}{\xi_4 p_{\text{ext}}} 2 q_0^{-k_1 - k_2} \text{B}\left(2k_2 - \frac{5}{2}, \frac{1}{2}\right). \quad (\text{E.21})$$